High Quality Factor Lamb Wave Resonators

Jie Zou

Electrical Engineering and Computer Sciences
University of California at Berkeley

Technical Report No. UCB/EECS-2014-216
http://www.eecs.berkeley.edu/Pubs/TechRpts/2014/EECS-2014-216.html

December 15, 2014

Acknowledgement

I would like to express my deepest appreciation to my advisor, Prof. Albert P. Pisano.I give my sincerest gratitude to Professor Clark T.-C. Nguyen for agree being reader of this research report. I would also like to thank Professor Liwei Lin, Prof. Richard M. White and Prof. Tsu-Jae King Liu for their valuable technical suggestions on this work.
I own my heartfelt appreciation to Dr. Chih-Ming Lin for his professional guidance. It was great joy to work in the Pisano Lab and I remain indebted to my former and current colleagues.
All devices studied in this report were fabricated at the Berkeley Marvell Nanofabrication Laboratory. I would like to thank all Nanolab staff for assisting me through these years.

High Quality Factor Lamb Wave Resonators

by

Jie Zou

A report submitted in partial satisfaction of the

requirements for the degree of

Master of Science

in

Engineering – Electrical Engineering and Computer Sciences

in the

Graduate Division

of the

University of California, Berkeley

Committee in charge:

Professor Albert P. Pisano, Chair
Professor Clark T.-C. Nguyen

Fall 2014

High Quality Factor Lamb Wave Resonators

by

Jie Zou

Research Project

Submitted to the Department of Electrical Engineering and Computer Sciences, University of California at Berkeley, in partial satisfaction of the requirements for the degree of **Master of Science, Plan II**.

Approval for the Report and Comprehensive Examination:

Committee:

Professor Albert P. Pisano
Research Advisor

(Date)

* * * * * * *

Professor Clark T.-C. Nguyen
Second Reader

(Date)

High Quality Factor Lamb Wave Resonators

Abstract

High Quality Factor Lamb Wave Resonators

by

Jie Zou

Master of Science in Electrical Engineering and Computer Sciences

University of California, Berkeley

Professor Albert P. Pisano, Chair

The small-in-size and CMOS compatible micro-electromechanical system (MEMS) resonators are likely to be the driving core of a new generation of devices such as radio frequency (RF) filters and timing references. Thanks to the CMOS compatibility, ability of high frequencies, low motional impedances (R_m), small frequency-induced drifts, and capability of multiple frequencies operation on a single chip, the aluminum nitride (AlN) Lamb wave resonators have attracted attention among various micromechanical resonator technologies. The lowest-order symmetric (S_0) Lamb wave mode in an AlN thin plate is particularly preferred because it exhibits high acoustic phase velocity, a low dispersive phase velocity characteristic, and a moderate electromechanical coupling coefficient.

In this report, basic analysis of the Lamb waves propagating in AlN and the device design techniques are presented in detail. Then, a novel technique to enhance the quality factor (Q) of Lamb wave resonator by utilizing an AlN plate formed in a butterfly shape is investigated in this paper. In the conventional design, the Q's of the micromachined Lamb wave resonators are largely harmed by the energy dissipation through the support tethers. The finite element analysis (FEA) simulation results show that the butterfly-shaped topology can efficiently change the displacement field in the AlN plate and reduce the vibration in the support tethers. The unloaded Q of the resonator is raised from 3,360 to 4,758 by simply using of the butterfly-shaped AlN plate with a tether-to-plate angle $\alpha = 59^{o}$, representing a 1.42× increase. The experimental Q's are also in good agreement with the anchor loss Q's computed using the PML-based FEA method.

_____

Professor Albert P. Pisano, Chair Date

ACKNOWLEDGEMENTS

First and foremost, I would like to express my deepest appreciation to my advisor, Prof. Albert P. Pisano. He gave me insightful suggestions in the research direction and large freedom to follow my own interest. He also gave me complete support and every opportunity in keep trying experiments and attending conferences to discuss with other researchers in the field. He is so warm and humorous that everybody likes him. His insights and personality are an excellent example of a great scientist and a great leader, and will benefit my whole life.

I give my sincerest gratitude to Professor Clark T.-C. Nguyen for agree being reader of this research report. I always admire his research on MEMS, analog circuits and RF communication. This report is also motivated from the theory he put forward. I would also like to express my sincere gratitude to Professor Liwei Lin, Prof. Richard M. White and Prof. Tsu-Jae King Liu for their valuable technical suggestions on this work.

I own my heartfelt appreciation to Dr. Chih-Ming Lin for his professional guidance on the AlN Lamb wave resonators, teaching me nanofabrication and all the invaluable discussions. It was great joy to work in the Pisano Research for Integrated Micromechanical & Electrical (PRIME) Systems Laboratory and I remain indebted to my former and current colleagues, Dr. Debbie Senesky and Dr. Jim C. Cheng, Dr. Ayden Maralani, Dr. Kristen Dorsey, Dr. Mitsutoshi Makihata, Dr. Nuo Zhang, Dr. Matilda Yun-Ju Lai, Dr. Fabian Goericke, Dr. Wei-Cheng Lien, Dr. Earnest Ting-Ta Yen, Dr. Matthew Chan, Dr. Sarah Wodin-Schwartz, Dr. Yegân Erdem, Kirti Mansukhani, Hongyun So, Anju Toor, Lilla Smith, Shiqian Shao, David Rolfe, Gordon Hoople, Maria Pace, Joy Xiaoyue Jiang, Levent Beker Ben Eovino, and John Herr for all the helpful discussions and your support. I also thank my friends Dr. Tsung-Chieh Lee and Le Zhang, for the discussions on the telecommunication technologies.

All devices studied in this report were fabricated at the Berkeley Marvell Nanofabrication Laboratory. I would like to thank all Nanolab staff for assisting me through these years.
At the same time, I wish to thank Hanyu Zhu, Zeying Ren, Xianling Liu, Chuang Qian, Bo Lv, Yang Yang, Yuping Zeng, Zheng Cheng, Taiki Hatakeyama and Ruonan Liu for giving me invaluable help and suggestions on MEMS fabrication.

Outside the academic environment, I would like to thank Yifan Jiang, Jun Xie, Wenwen Jiang, Weixi Zhong, Minghui Zheng, Xiao Liang, Meng Cai, Xuance Zhou, Siyuan Xin, Chang Liu, Ming Tin, Junkai Liu, Bo Xu, Fan Yang, Qianyi Li, Yuchen Pan, Yuan Ma and Qi Wang. With their company in the United States, I have a wonderful and enjoyable life outside the work environment.

Last but not the least, I owe more than words can describe to my parents and my fiancé, Guanbin Zou, Fenglian Zeng and Pucong Han, for their never ending love and unequivocal dedication. I reserve my sincere gratitude to your patience, your companionship, and your steadfast encouragement.

TABLE OF CONTENTS

Chapter 1

Introduction

Microelectromechanical systems (MEMS), inspired by microelectronics and benefited from the development of microfabrication technology, have been recently intensively researched and successfully commercialized in many fields of technology. The conventional MEMS technology which converts energy from mechanical to electrical domain or vice versa – sensors and actuators, play an irreplaceable role in people's modern life and are offered by many suppliers today. In contrast to their unique function, radio frequency microelectromechanical systems (RF MEMS) process electrical signal just like electronics using mechanically vibrating structure, and have replaced on-chip electrical RF devices to provide frequency control functions due to their extraordinary performance compared to on-chip electrical counterparts. With small size, high performance and Complementary metal–oxide–semiconductor (CMOS) compatibility, RF MEMS resonators offer promising building blocks for frequency control and timing reference in contemporary RF front-end in wireless communication systems.

This chapter starts by introducing the potential application of MEMS resonators in bandpass filters and oscillators in the current RF front-end transceivers and novel reconfigurable channel-select RF front-end architectures. Technical requirements for MEMS resonators will be summarized followed by short descriptions of existing MEMS resonator technologies.

1.1 MEMS Resonators for RF Front-End Technology

1.1.1 Current and Future RF Front-End Transceivers

Figure 1–1 shows the system block diagram of a state-of-art quad-band super-heterodyne receiver (Rx) architecture in cellular phones. The off-chip SAW filters and quartz crystal resonators are the main components for frequency selection and time reference. With the development of MEMS technology, mechanical vibrating structures used for frequency control and time keeping can be fabricated on Si wafers with excellent performance, tiny size, low power consumption, and CMOS compatibility. In order to reduce complexity of integration, cost and power consumption in next-generation

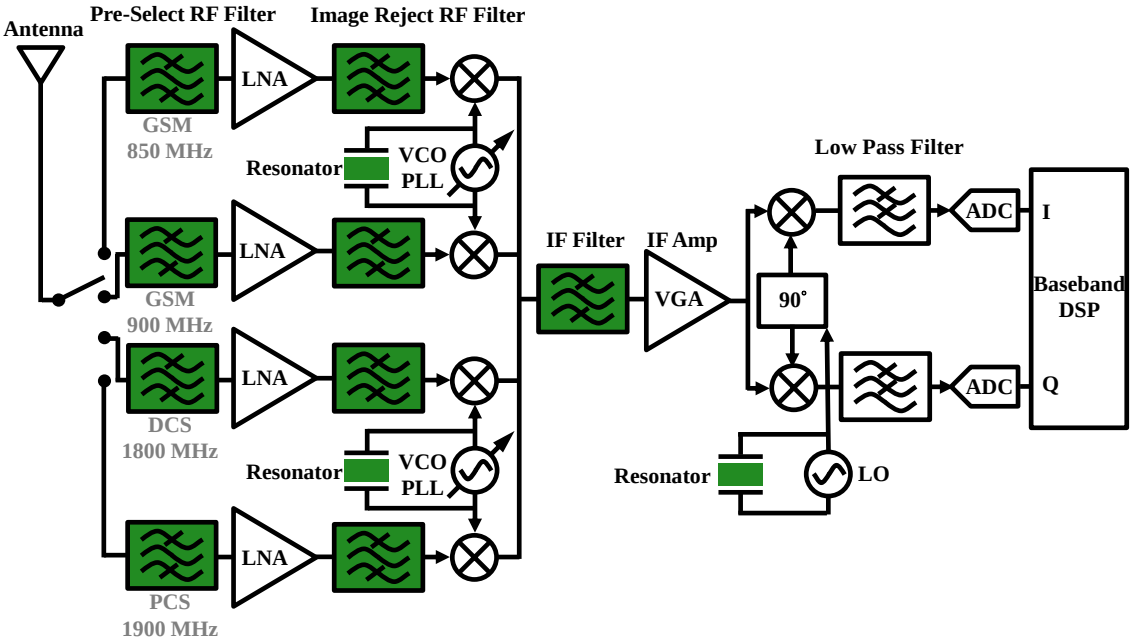

Figure 1-1. System block diagram of a quad-band super-heterodyne receiver (potential MEMS resonator replacements are shaded).

communication systems, CMOS compatible MEMS resonators are considered as direct replacements of these discrete components. As is indicated in the shaded area in Figure 1-1, the receiver front-end architecture can adapt MEMS resonator technology to realize a highly integrated system.

In addition, novel RF frond-end channel-select architecture is proposed by Nguyen to use the high *Q* MEMS resonator technology to eliminate the use of the RF low noise amplifiers (LNAs) and transistor mixers, thereby significantly reduce the complexity of integrated circuit (IC) and lower the power consumption [15]. In the circuit of Fig. 1–2 (a), the key feature of the RF channel-select architecture is the closely spaced filter bank paired with low loss switched to eliminate not only out-of-band interferers but also out of channel interferers [16]. For a narrowband filter, the insertion loss heavily depends on the resonator *Q* while a small percent bandwidth is needed [17], [18].

One step further, as the increasing desire for reconfigurable radios capable of adapting to any communication standard has spurred great interest in the concept of a software defined radio (SDR), Nguyen pointed out that MEMS devices can be used in massive numbers as the way of transistors [2008]. He put forward the software defined radio front-end utilizing a micromechanical RF channel-select filter network to realize a frequency gating function, as is shown in Figure 1-2 (b). Large numbers (>100) of switchable MEMS filters are used to realize the programmable frequency gate instead of restricting the implementation of a programmable frequency gate to a single tunable filter.

All the above information reveals that CMOS compatible, high-*Q*, low-impedance, thermally stable and frequency tunable micromechanical resonators are essential to

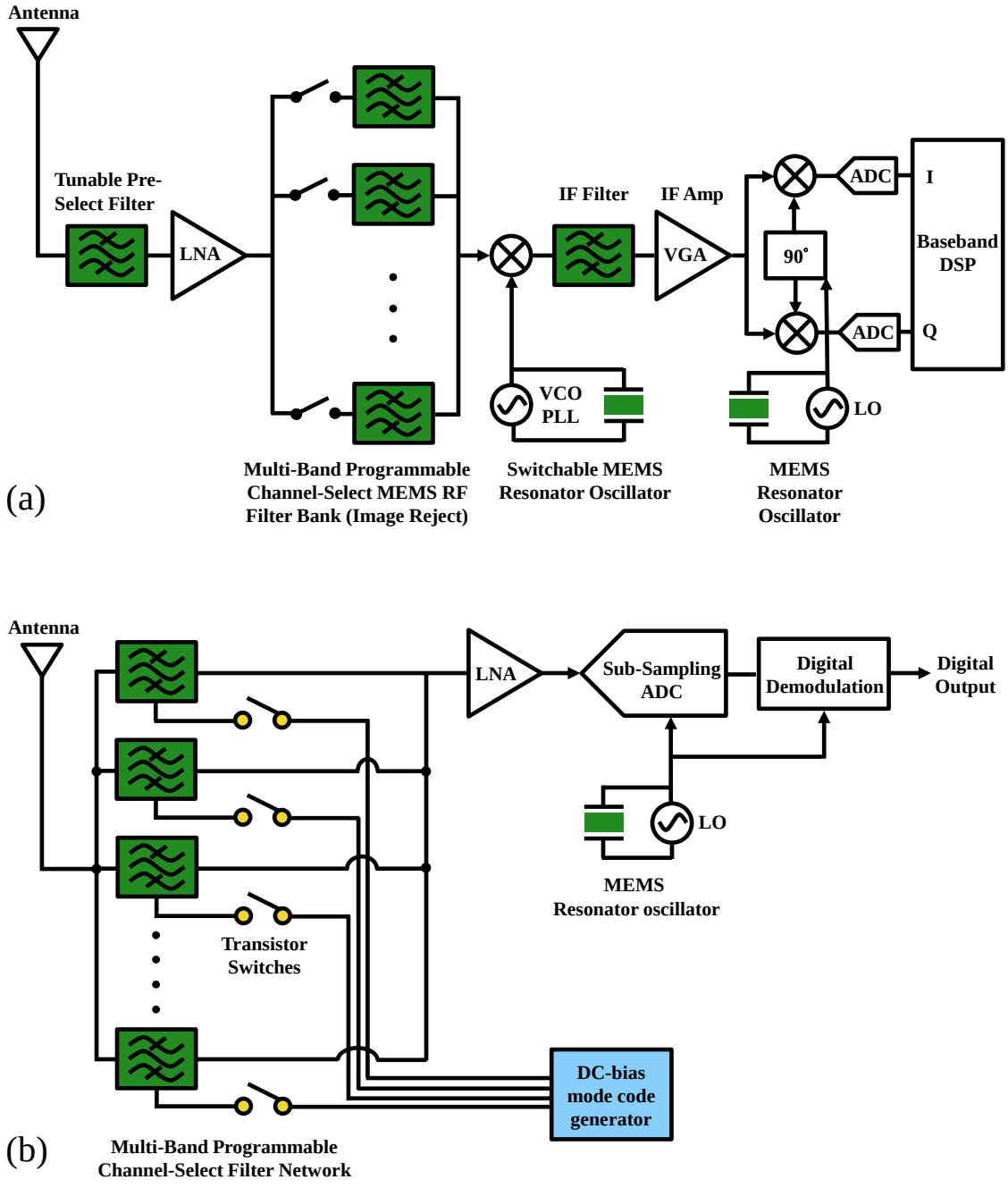

Figure 1-2. System block diagrams for (a) a channel-select receiver architecture using integrated MEMS filter bank and resonators, and (b) a highly-reconfigurable, low-power SDR front-end receiver utilizing a network of large numbers of MEMS RF filters to realize a frequency gating function. (RF MEMS devices are shaded in green).

construct single-chip transceiver in the near future and the highly configurable SDR front-end in the long run.

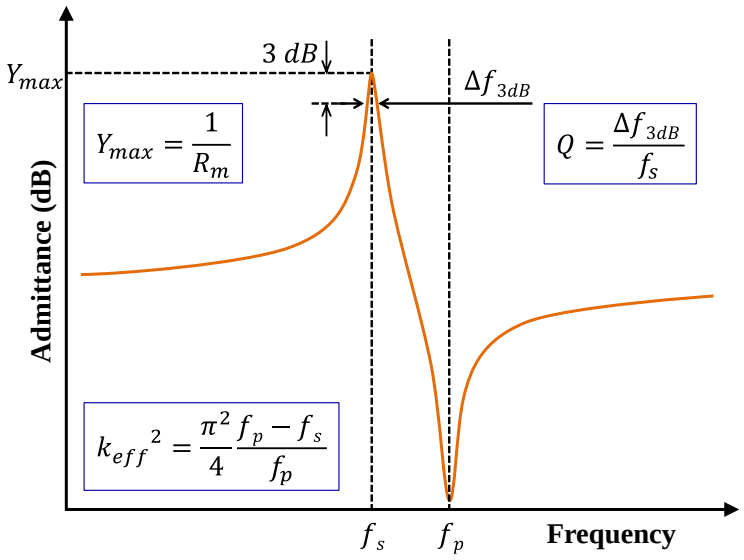

Figure 1-3. A typical frequency response of a resonator with definitions of important parameters.

1.1.2 Resonator Parameters

Before talking about specific applications, a brief introduction to the general parameters of a resonator is given here. As shown in Figure 1-3, a typical frequency response of the admittance has a resonance and an anti-resonance peak, and the definitions of important parameters are listed below:

The quality factor characterizes the sharpness of the resonance peak and is defined by the ration of the 3dB bandwidth to the resonance frequency:

$$Q = \frac{\Delta f_{3dB}}{f_s}. \tag{1.1}$$

The effective coupling coefficient physically represents the energy conversion efficiency of the device and is defined by the distance between the resonance and anti-resonance peaks:

$$k_{eff}^2 = \frac{\pi^2}{4}\frac{f_p - f_s}{f_p}. \tag{1.2}$$

The motional impedance represents the loss level when the device is in resonance:

$$R_m = \frac{1}{Y_{max}}. \tag{1.3}$$

The temperature coefficient of frequency represents the amount of frequency shift when temperature changes:

$$TCF = \frac{df}{dT}\frac{1}{f}. \tag{1.4}$$

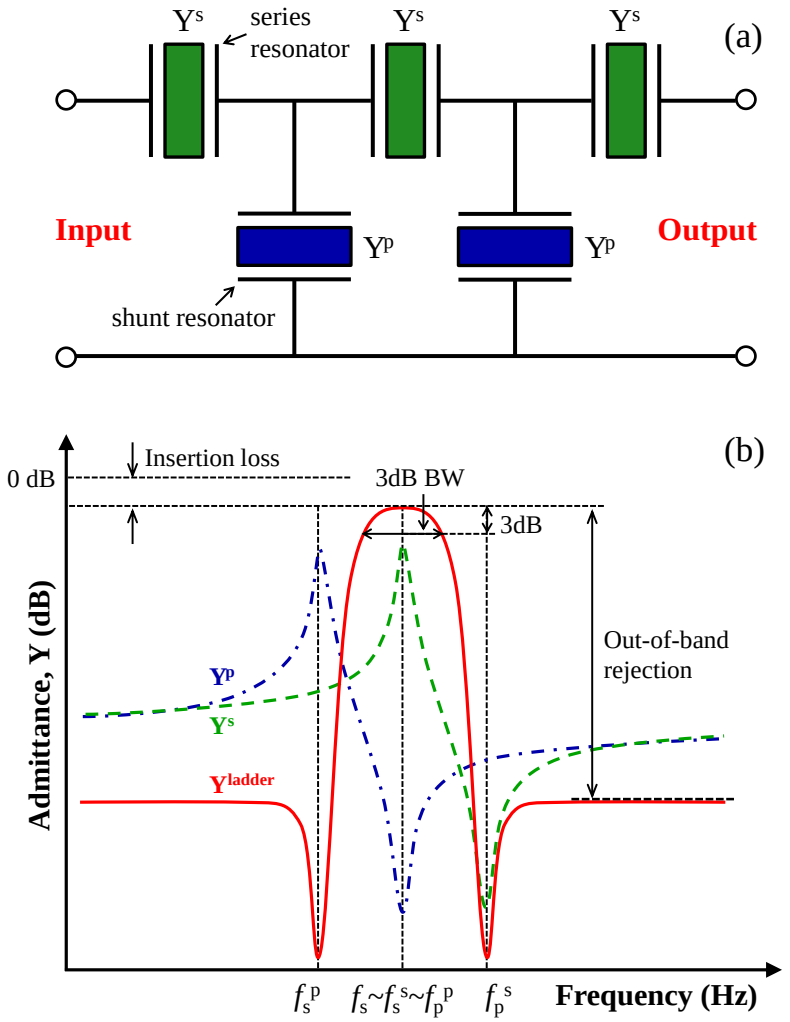

Figure 1-4. (a) Simple ladder filter with micromechanical resonators in the series and shunt branches and (b) the typical frequency spectrum of the synthesized ladder filter and common parameters for evaluating the filter.

More introductions of these important parameters will be given in detail in the later chapters when analyzing specific ones.

1.1.2 MEMS Resonators for Bandpass Filters

In the front-end of wireless communication systems, bandpass filters are used to block out the unwanted signals. Figure 1–4 (a) shows a common electrically coupled filter, a ladder filter configuration, employing resonators in both series and shunt branches [1], [2], [20]. All the resonators in the series branch have the same series and parallel resonance frequencies (f_s and f_p). Similarly, the resonators in the shunt branch have the identical series resonance frequency differing from the series resonance frequency of the resonators in the series branch.

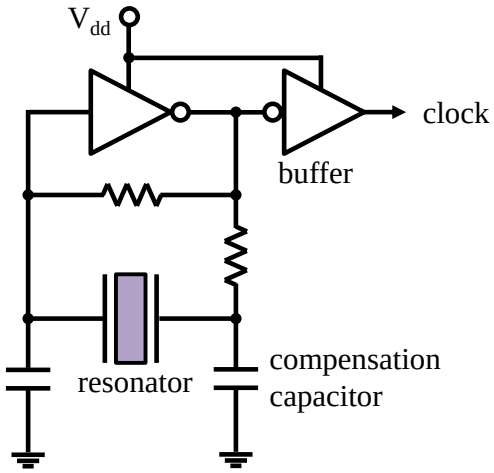

Figure 1-5. Simple illustration of a Pierce oscillator using crystal or ceramic resonators.

A typical frequency response of the ladder filter is shown in Fig. 1–4 (b). Of special interest are the in-band insertion loss, 3dB bandwidth (BW), out-of-band rejection, the skirts, and the shape factor. As is indicated in Figure 1-4 (b), the 3dB BW is usually set by the effective coupling coefficient (k_{eff}^2) of the series and shunt resonators. To minimize the insertion loss of the ladder filter, the shunt resonators should have high Q and large impedance at their parallel resonance frequency f_p^p and the series resonators have high Q and low impedance (R_m) at their series resonance frequency f_s.

1.1.3 MEMS Resonators for Frequency References

Time references are employed in almost all electronic systems to keep track of real time and set precise clock frequency for digital data transmission. As shown in Fig. 1–5, a simple Pierce oscillator consists of a resonator – nowadays mostly quartz crystal or ceramic resonator, a positive feedback transistor, and an output buffer amplifier. The oscillator circuit locks oscillation by taking a voltage signal from the resonator, amplifying it, and then feeding it back to the resonator. So for the employed resonator the low loss (high Q) and temperature stability (low TCF) are of special importance for this application.

To summarize, high Q is a universally highly desirable property in the MEMS resonators for RF front-end applications to further enable low-loss and stable filters and low-phase-noise oscillators. Besides that, large k_{eff}^2, low R_m, ability of high frequency are special important technical challenges for filters and low TCF, impedance matching and capability of high frequency are essential for oscillator applications.

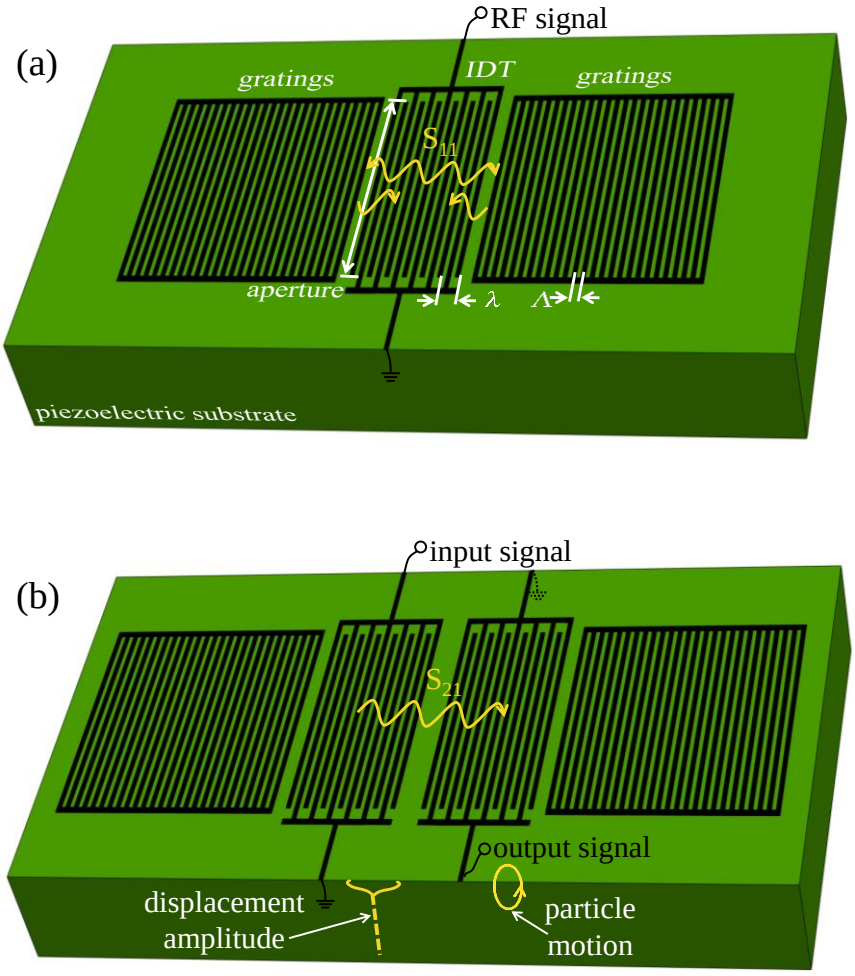

Figure 1-6. Illustration of (a) one-port and (b) two-port SAW resonators.

1.3 MEMS Resonators

MEMS resonators can be sorted into piezoelectric and capacitive transduced ones. Generally, the piezoelectric MEMS resonators tend to show a large coupling coefficient and the capacitive resonators have a super high *Q* but a small coupling coefficient. We will introduce the piezoelectric resonators in detail here (SAW, BAW, LWR) and then a brief introduction to the capacitive resonators.

1.3.1 Surface Acoustic Wave (SAW) Resonator

SAW resonators have been dominating the market for RF filters for several decades. A lot of research has been done in the 19th and 20th centuries after Rayleigh discovered

surface acoustic waves propagating in solids in 1885 [28]. Although it remained a scientific curiosity with very few applications for a long time, the direct generation and detection of surface elastic waves through the piezoelectric effect led to a breakthrough in SAW devices after the invention of an interdigital transducer (IDT) by White and Voltmer in 1965 [29]. SAW devices have been widely used as IF and RF filters in wireless transmission systems for several decades because of their small size, low cost, and great performance.

Figure 1-6 shows the schematic of one-port and two-port SAW resonators composed from piezoelectric substrate, IDT pairs, and gratings. The IDT finger width is usually equal to quarter wavelength (λ/4) so the interdigital electrode pitch (Λ) as well as the grating period equal half wavelength (λ/2). SAWs can be generated by applying RF signals to the IDT and propagate on the surface of the substrate along the direction perpendicular to the fingers. The generated SAWs would be reflected by the gratings at both sides to reduce the energy loss.

The most severe limitation for SAW devices is that they can hardly achieve frequencies above 2.5 GHz. SAW phase velocities of common piezoelectric substrates, such as quartz, $LiNbO_3$, and $LiTaO_3$, are below 4,000 m/s, and the optical lithography today can only achieve 0.25um line-width. Even when the frequency approaches 2G, the shrinkage of the IDT comb-fingers makes SAW resonators vulnerable to electrostatic discharge. Therefore, the *Q* factor is typically lower than 400. What's more, the required piezoelectric substrate is not compatible with standard microelectronic manufacturing.

1.3.2 Bulk Acoustic Resonator (BAW)

BAW resonators utilize the acoustic waves propagating through the bulk of a material, including longitudinal wave, shear horizontal (SH) wave, and shear vertical (SV) wave. The longitudinal acoustic wave is also called P-wave (primary wave) and has the highest phase velocity. BAW resonators mostly utilize the longitudinal mode or the thickness shear mode.

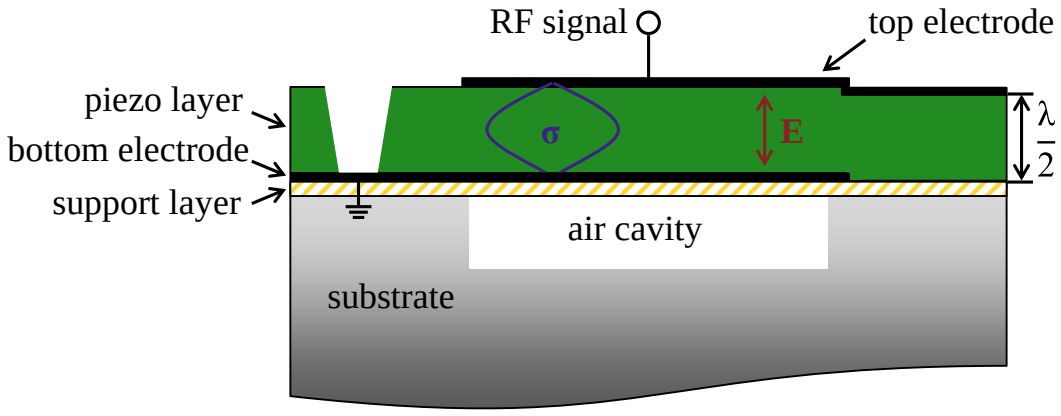

Figure 1-7. Illustration of the cross section of a simple FBAR.

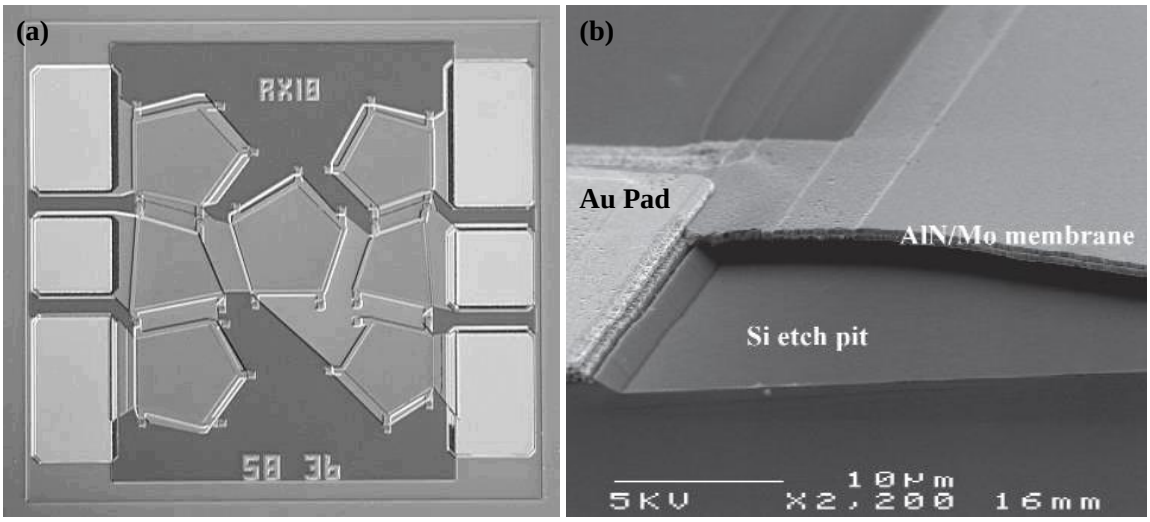

Figure 1-8. (a) A top view of a filter composed of three series and four shunt FBARs [27] and (b) the side view of the AIN membrane stretching over a micro-machined silicon pit [28].

A thin-film BAW resonator is a device composed mainly from a piezoelectric thin film surrounded by two metal electrodes that generate the longitudinal wave propagating according to a thickness extension mode (TE). There are mainly two ways for the wave to be trapped in the resonator, which differentiates the two type of devices that have reached volume manufacturing today: the FBAR and SMR.

1.3.2.1 Film Bulk Acoustic Resonator (FBAR)

As is shown in Figure 1-7, the FBAR is a free-standing piezoelectric membrane sandwiched between top and bottom electrodes. It uses air-solid interfaces both over and underneath the resonating film, and the air gap enables a high reflectance of the acoustic waves and thus a high *Q*. It can be manufactured over a sacrificial layer, released through isotropic etching, or by etching part of the substrate underneath the resonator. Common applications using FBAR technology are filters and duplexers at 1.9 GHz for cellular phones.

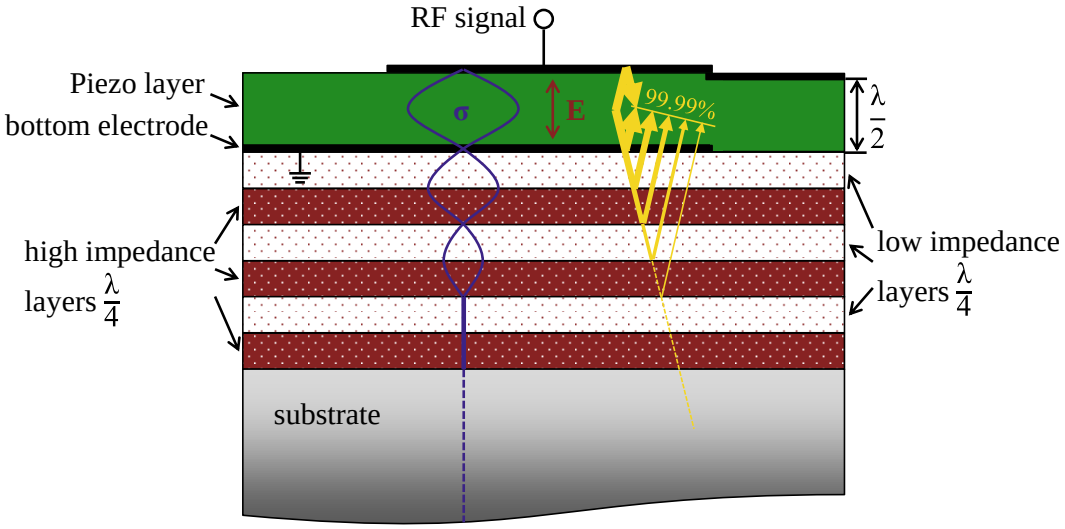

Figure 1-9. Schematic of the cross section view of a SMR.

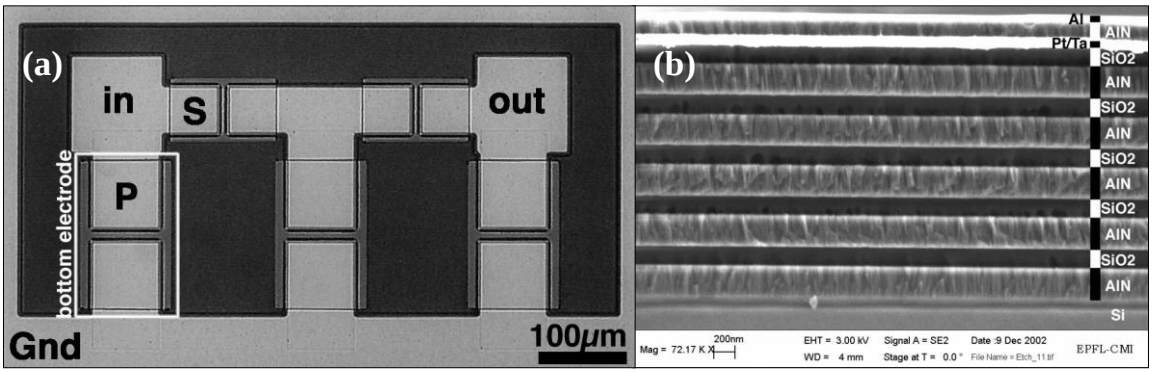

Figure 1-10. (a)Top view of a 2-stage π ladder filter and the (b) cross-section view of five reflector stacks of the SMR [26].

1.3.2.2 Solidly Mounted Resonator (SMR)

The SMR is a more robust structure where the top interface is also of the air-solid type, but solidly mounted to the substrate using a Bragg reflector stack, as is shown in Figure 1-9. An efficient isolation is performed by a set of quarter-wavelength sections of materials with different acoustic impedance. The larger the difference, the more efficient is the reflection. For example, the use of AlN and SiO_2 requires at least nine alternating layers, whereas replacing AlN by tungsten allows this number to be reduced down to five. This non-free-standing structure provides physical robustness and good power handling capability.

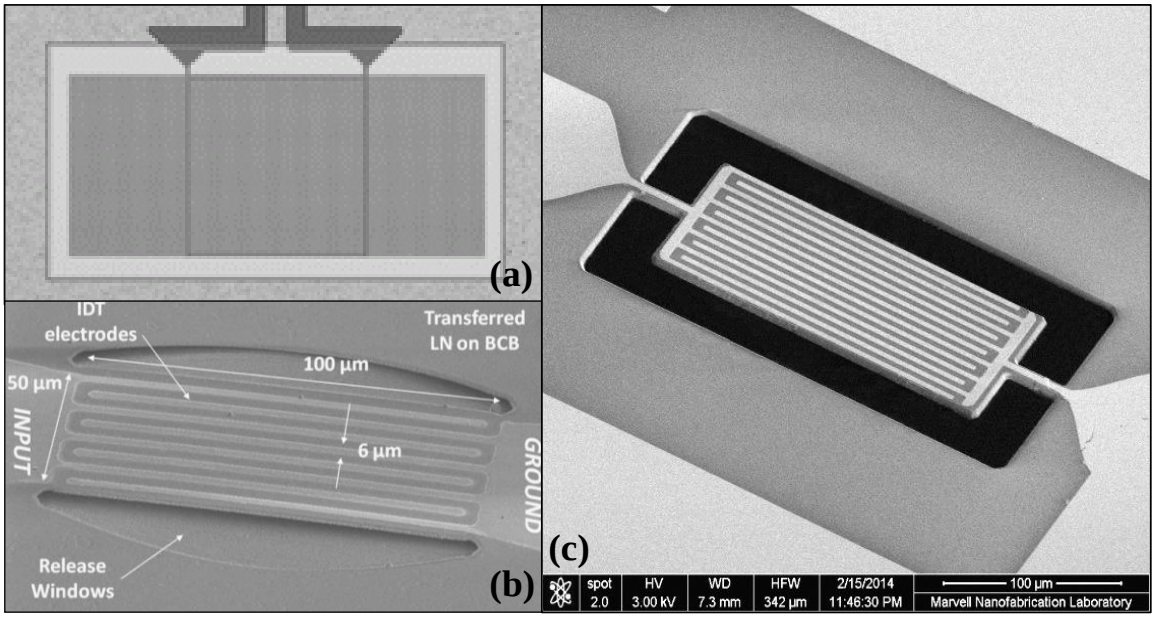

Figure 1-11. Lamb wave resonators (a) with reflectors, (b) using edge reflectors on $LiNbO_3$ and on (c) AlN membranes.

1.3.3 Lamb Wave Resonator (LWR)

AlN Lamb wave resonator (Contour mode resonator) technology was brought up by Piazza and Yantchev since 2002. The structure of Lamb wave resonator combines SAW resonator and FBAR, so it enjoys both advantages from these two mature technologies: it is transduced by IDTs so the frequency is lithography defined; the suspended structure enables a higher *Q* and larger phase velocity. What's more, AlN process technology can be CMOS compatible and can employ the maturity developed for FBAR and SMR. From the acoustic perspective, the lowest-order symmetric (S_0) Lamb wave mode in an AlN thin plate exhibits its phase velocity close to 10,000 m/s, a low dispersive phase velocity characteristic, and a moderate electromechanical coupling coefficient. That is to say, the AlN LWRs are able to the low resonance frequency limitation and integration problem faced by SAW resonators, and the multiple frequency capability problem faced by piezoelectric BAW resonators.

As presented in Fig. 1–11 (a), one topology of the LWR is based on the reflection from periodic grating reflectors like used in SAW devices. Another topology is based on the reflection from suspended free edges of the thin plate as depicted in Fig. 1–15 (b).and (c), where (b) shows LWR based on transferred $LiNbO_3$ film and (c) presents LWR based on sputtered AlN film and released by XeF_2. Lamb wave modes are generated by IDTs and then propagate in the AlN thin plate until reflection at both sides. Lamb wave conversion does not occur at periodic gratings but possibly upon reflection at the suspended free edges [60]. Fortunately, the lowest-order Lamb wave modes mostly used in LWRs don't exhibit mode conversion upon reflection at the suspended free edges.

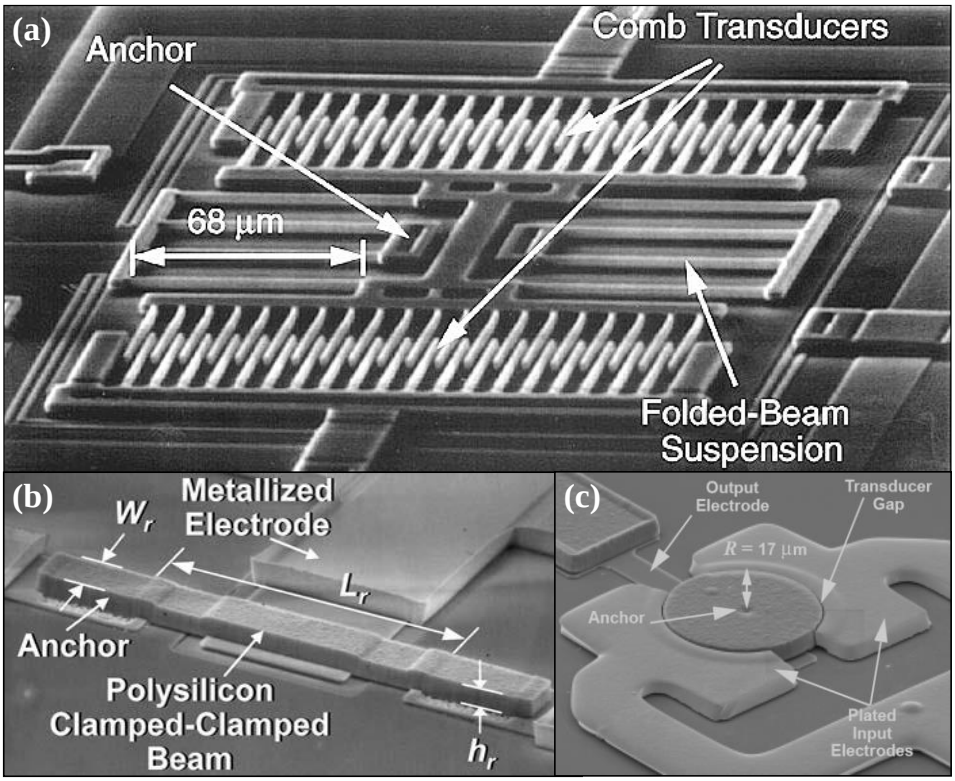

Figure 1-12. SEM image of (a) a capacitively transduced comb-drive resonator, (b) a poly-Si clamped-clamped beam flexural-mode resonator and (c) an electrostatic disk micromechanical resonator.

1.3.4 Electrostatic Resonators

The first electrostatic vibrating comb-driven resonator on poly crystalline was reported by Tang *et al.* in 1989 [13]. As shown in Fig. 1–12 (a), the capacitive-comb transduced resonator consists of a finger-supporting shuttle mass suspended above the substrate by folded flexures, which are anchored to a ground plane on the substrate. In 2000, as shown in Fig. 1–10 (b), Clark *et al.* proposed a new micromechanically vibrating disk resonator. Based on the radial contour mode, the micromechanical disk structure can attain very high frequencies while retaining relatively large dimensions because the high stiffness of the disk structure.

The transduction is based on the electrostatic force across a sub-micron dielectric gap. These electrostatic resonators typically have very high quality factors so they are among the excellent solutions to replace quartz resonators in reference clock circuits. However their electromechanical coupling is usually small and motional impedance is too high (up to several thousands ohms) that their interface with 50-ohm systems is very difficult for applications for RF filters.

1.4 Report Outline

This report is organized into five chapters about the AlN RF telemetry components. Chapter 1 contains the research motivation, technical challenges, and existing solutions. Chapter 2 provides the fundamentals of propagating characteristics of Lamb wave modes in AlN membranes. Resonator basics, design, modeling, and fabrication process are presented in Chapter 3. Chapter 4 focuses on the analysis, design, simulation and testing result of high *Q* AlN LWRs using butterfly-shaped plates. Finally, Chapter 5 will conclude this research work.

Chapter 2
Lamb Wave propagating in AlN film

Piezoelectric thin films have been utilized in SAW and BAW filters mainly because of the efficient electromechanical transduction. Lamb wave in piezoelectric thin plates has drawn great attentions due to its high phase velocity. In this chapter, a study of the lowest-order Lamb wave modes (S_0 modes) in an AlN plate is presented. Phase velocities, electromechanical coupling coefficients, and dispersion characteristics of TCF of Lamb waves will be included in the theoretical studies.

2.1 Aluminum Nitride (AlN)

AlN emerged as the most suitable technology for the transduction of acoustic waves for RF applications because it is an excellent compromise between performance and manufacturability. Although its coupling coefficient is not as high as that of ZnO, PZT or $LiNbO_3$, it has high acoustic velocity, high thermal conductivity, low acoustic loss,

Table 2-1. Physical properties of ZnO, AlN, and $LiNbO_3$ [27].

	ZnO	**AlN**	**$LiNbO_3$**	**Units**
Density	5680	3260	4700	(kg/m^3)
Longitudinal acoustic wave velocity	~6350	~11300	~6550	(m/s)
Shear acoustic wave velocity	~2720	~6000	~3590	(m/s)
Lattice constant, *c*	3.249	3.112	13.863	(Å)
Lattice constant, *a*	5.206	4.982	5.150	(Å)
Piezoelectric coefficient, e_{15}	–0.48	–0.48	3.69	(C/m^2)
Piezoelectric coefficient, e_{31}	–0.57	–0.58	0.3	(C/m^2)
Piezoelectric coefficient, e_{33}	1.32	1.55	1.77	(C/m^2)
Thermal expansion (300 K)	2.92	4.15	5~15	(10^{-6}/°C)
Thermal conductivity	60	280	5.6	(W/mK)
TCF	–60	–25	–58~-90	(ppm/°C)

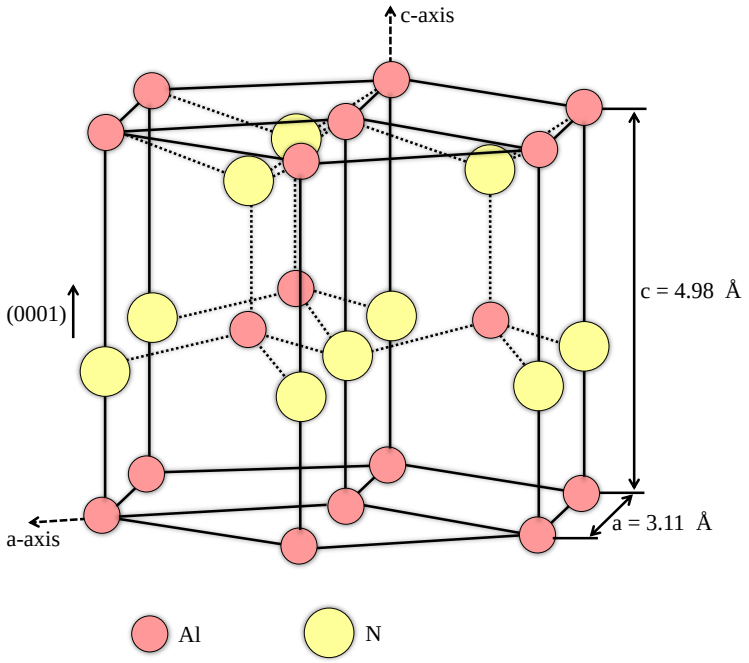

Figure 2-1. Hexagonal wurtzite crystal structure of AlN.

chemical stability and relatively low TCF, as is shown in Table 2-1. These properties enable the MEMS resonators featuring the ability of high frequency, excellent power handling capability, high *Q*, functionality in harsh environment, and limited drift with temperature.

As illustrated in Fig. 2–1, AlN is wurtzite-structured material with *c*-axis, belonging to hexagonal crystal system, with polarized direction along the *c*-axis (0001) which is usually normal to the substrate.

Another advantage of AlN is the low process temperature and the fact that it does not contain any contaminating elements harmful for semiconductor devices, unlike most other piezoelectric materials. This is essential in the case of monolithic integration of MEMS resonators with microelectronic integrated circuits. Reactive sputtering from a pure Al target in a plasma containing nitrogen is the most suitable method to obtain crystalline AlN films with sufficient quality for MEMS resonator applications at a deposition temperature lower than 400℃. Figure 2-2 shows the cross section of such an AlN film grown in pulsed DC mode. The microstructure is typical, with very densely packed columnar grains. The parameters of the AlN deposition process have to be optimized in order to ensure that a vast majority of grains are oriented along the c-axis since the spontaneous polarization of AlN, and hence the maximum piezoelectric effect, is parallel to that direction.

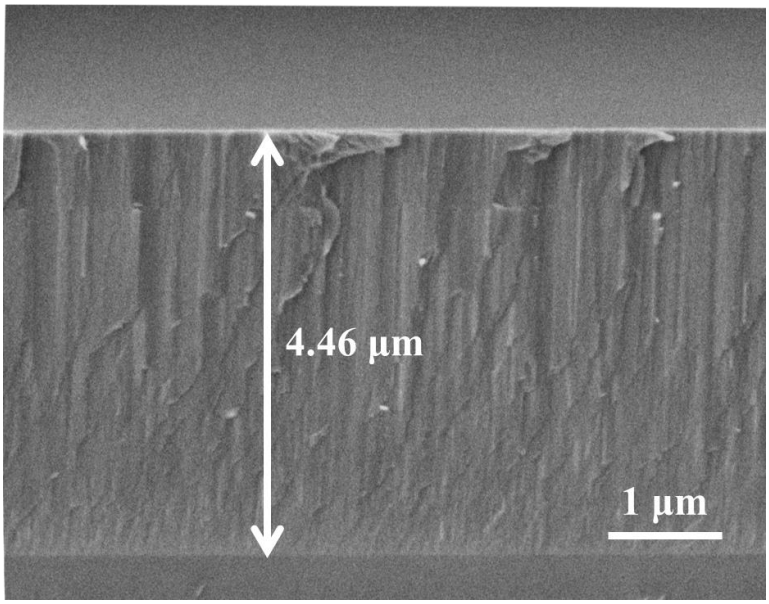

Figure 2-2. Hexagonal wurtzite crystal structure of AlN.

2.2 Piezoelectric Effect and its Constitutive Equations

"Piezoelectricity" is derived from the Greek word "piezein", meaning "to press", meaning that crystal that acquire charge when being compressed, twisted, or distorted are said to be piezoelectric. The physical origin of piezoelectricity comes from the charge asymmetry within the primitive unit cell which results in the formation of a net electric dipole. The polar axis is an imaginary line pointing through the center of the negative and positive charge in the dipole. As is shown in Figure 2-3 is examples of how the piezoelectricity (here the piezoelectric strain parameter d-coefficients are used) relates the force and charge of a piezoelectric block.

In the mechanical domain of a linear elastic material the Hooke's Law dominates:

$$T = cS \text{ or } S = sT, \tag{2.1}$$

where c is the elastic stiffness constant, s is the elastic compliance constant, T and stress tensor and S is the strain tensor.

In the electrical domain, the dielectric constant relates the charge density displacement vector D and electric field vector E,

$$D = \varepsilon E \text{ or } E = \beta D, \tag{2.2}$$

Where ε is the dielectric permittivity constant and β is the dielectric impermittivity constant.

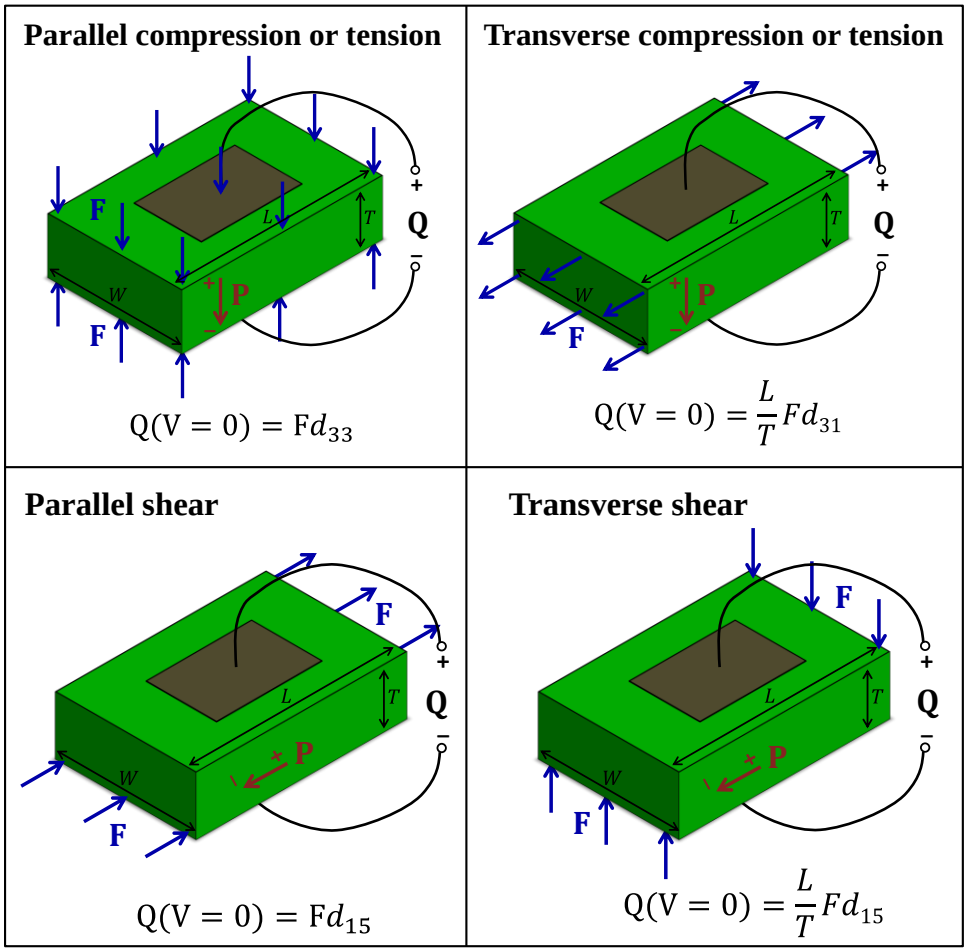

Figure 2-3. A piezoelectric brick with different piezoelectric actuation modes (d_{33}. d_{31}, d_{15} actuation with different pole and force direction).

Like mentioned before, piezoelectricity combine the mechanical and electrical behavior of the material. Normally there are four types of piezoelectric coefficient: h, d, g, e, among which d and e form are most widely used because they directly relate the stress and strain tensors. We have talked about the d piezoelectric coefficient before, and the e form equations are used for calculation in this report. The e-form constitutive equation is:

$$\begin{cases} T = c^E S - e^T E \\ D = \varepsilon^S E + eS \end{cases}, \tag{2.3}$$

where the superscripts E and S in the stiffness constant and the dielectric constant denote that they are measured at constant electric field and constant strain, but the superscript T in the piezoelectric constant e denotes the transport of the matrix.

Since AlN like most piezoelectric medium is with hexagonal symmetry, the constitutive equations can be simplified to:

$$\begin{bmatrix} T_1 \\ T_2 \\ T_3 \\ T_4 \\ T_5 \\ T_6 \end{bmatrix} = \begin{bmatrix} c_{11} & c_{12} & c_{13} & 0 & 0 & 0 \\ & c_{11} & c_{12} & 0 & 0 & 0 \\ & & c_{33} & 0 & 0 & 0 \\ & & & c_{44} & 0 & 0 \\ & & & & c_{44} & 0 \\ & & & & & c_{44} \end{bmatrix} \begin{bmatrix} S_1 \\ S_2 \\ S_3 \\ S_4 \\ S_5 \\ S_6 \end{bmatrix} - \begin{bmatrix} 0 & 0 & e_{31} \\ 0 & 0 & e_{31} \\ 0 & 0 & e_{33} \\ 0 & e_{15} & 0 \\ e_{15} & 0 & 0 \\ 0 & 0 & 0 \end{bmatrix} \begin{bmatrix} E_1 \\ E_2 \\ E_3 \end{bmatrix}, c_{66} = \frac{c_{11}-c_{12}}{2} \quad (2.4)$$

$$\begin{bmatrix} D_1 \\ D_2 \\ D_3 \end{bmatrix} = \begin{bmatrix} \varepsilon_1 & 0 & 0 \\ & \varepsilon_1 & 0 \\ & & \varepsilon_3 \end{bmatrix} \begin{bmatrix} E_1 \\ E_2 \\ E_3 \end{bmatrix} + \begin{bmatrix} 0 & 0 & 0 & 0 & e_{15} & 0 \\ 0 & 0 & 0 & e_{15} & 0 & 0 \\ e_{31} & e_{31} & e_{33} & 0 & 0 & 0 \end{bmatrix} \begin{bmatrix} S_1 \\ S_2 \\ S_3 \\ S_4 \\ S_5 \\ S_6 \end{bmatrix}. \quad (2.5)$$

Similar to the d-coefficient, the e3l term maps the thickness electric field to contour stress or maps the contour train to thickness charge flux, and e33 maps thickness electric field to thickness stress or thickness strain to thickness charge flux.

The coefficient of stiffness matrix (c), piezoelectric stress (e) matric, piezoelectric strain matrix (d), and the dielectric matrix of the AlN film used in calculation in this report are listed below:

$$[c] = \begin{bmatrix} 3.45 & 1.25 & 1.20 & 0 & 0 & 0 \\ 1.25 & 3.45 & 1.20 & 0 & 0 & 0 \\ 1.20 & 1.20 & 3.95 & 0 & 0 & 0 \\ 0 & 0 & 0 & 1.18 & 0 & 0 \\ 0 & 0 & 0 & 0 & 1.18 & 0 \\ 0 & 0 & 0 & 0 & 0 & 1.10 \end{bmatrix} (10^{11}\ \mathrm{N/m^2}), \quad (2.6)$$

$$[e] = \begin{bmatrix} 0 & 0 & 0 & 0 & -0.48 & 0 \\ 0 & 0 & 0 & -0.48 & 0 & 0 \\ -0.58 & -0.58 & 1.55 & 0 & 0 & 0 \end{bmatrix} (\mathrm{C/m^2}), \quad (2.7)$$

$$[d] = \begin{bmatrix} 0 & 0 & 0 & 0 & -4.068 & 0 \\ 0 & 0 & 0 & -4.068 & 0 & 0 \\ -2.646 & -2.646 & 5.532 & 0 & 0 & 0 \end{bmatrix} (10^{-12}\ \mathrm{m/V}) \quad (2.8)$$

$$[\varepsilon] = \begin{bmatrix} 8.0 & 0 & 0 \\ 0 & 8.0 & 0 \\ 0 & 0 & 9.5 \end{bmatrix} (10^{-11}\mathrm{F/m}). \quad (2.9)$$

2.3 Solid Acoustic Wave Properties

The acoustic wave propagating in solids are generally two types: bulk acoustic wave and solid acoustic wave. Bulk acoustic waves travel in the bulk of solid materials,

including longitudinal waves and shear waves, while surface acoustic wave can only travel along the surface of materials. The longitudinal wave is when the particle vibration is in the direction of wave propagation. The shear velocity is when the vibration is perpendicular to the propagation direction of the wave.

Given the material properties of piezoelectric materials and the propagation direction of acoustic waves, the stiffen Christoffel matrix approach can be utilized to solve for the phase velocity and piezoelectric coupling constant (k^2) of a specific acoustic wave mode.

By solving the Christoffel equation, we can obtain the longitudinal wave with phase velocity:

$$v_L = \sqrt{\frac{c_{11}}{\rho}}. \tag{2.10}$$

For AlN with the material properties listed in Table 2-2, the v_L=10287.28 m/s.

We can also obtain one pure shear mode with phase velocity:

$$v_{PS} = \sqrt{\frac{c_{66}}{\rho}}, \tag{2.11}$$

and one stiffen shear mode with phase velocity:

Table 2-2. Material constants of AlN used in the calculations

	Symbol	AlN	Units
Stiffness constants	C_{11}	345	(10^9 N/m^2)
	C_{12}	125	
	C_{13}	120	
	C_{33}	395	
	C_{44}	118	
	C_{66}	110	
Mass density	ρ	3260	(kg/m^3)
Piezoelectric constants	e_{15}	–0.48	(C/m^2)
	e_{31}	–0.58	
	e_{33}	1.55	
Dielectric constants	ε_{11}	8.0	(10^{-11} F/m)
	ε_{33}	9.5	

$$v_{SS} = \sqrt{\frac{c_{44}+\frac{e_{15}^2}{\varepsilon_{11}}}{\rho}}, \tag{2.12}$$

$$k^2 = \frac{e_{15}^2}{c_{44}\varepsilon_{11}}. \tag{2.13}$$

For AlN with properties listed in Table 2-2, the pure slow shear mode has the phase velocity 5597 m/s, and the fast shear mode has the phase velocity 5867 m/s with k^2 2.45%. Therefore, the (2000) AlN membranes provide a pure fast shear mode.

Following the similar approach as developed by Campbell, the matrix method is effectively employed. The Rayleigh wave only propagates at surfaces. The Rayleigh velocity is often approximated by:

$$v_R \cong \frac{0.87+1.12\gamma}{1+\gamma} v_S, \tag{2.14}$$

where γ is the Poisson ration, and

$$\frac{v_L}{v_S} = \sqrt{\frac{c_{11}}{c_{44}}} = \sqrt{\frac{1-\gamma}{\frac{1}{2}-\gamma}}. \tag{2.15}$$

For piezoelectric materials the phase velocity of propagation of acoustic waves is higher than that in the non-piezoelectric case, since the effective stiffness is enhanced by the piezoelectric stress term, namely piezoelectric stiffening:

$$c_{eff}^E = c^E + \frac{e^2}{\varepsilon^2}. \tag{2.16}$$

Therefore, the unstiffened phase velocity and piezoelectric stiffened phase velocity of a material are:

$$v_{unstiffened} = \sqrt{\frac{c^E}{\rho}}, \tag{2.17}$$

$$v_{stiffened} = \sqrt{\frac{c_{eff}^E}{\rho}} = \sqrt{\frac{c^E+\frac{e^2}{\varepsilon^2}}{\rho}} = v_n\sqrt{\frac{1}{1-k^2}}, \tag{2.18}$$

where the k^2 is the electromechanical coupling coefficient:

$$k^2 = \frac{e^2}{\varepsilon^S c^D}. \tag{2.19}$$

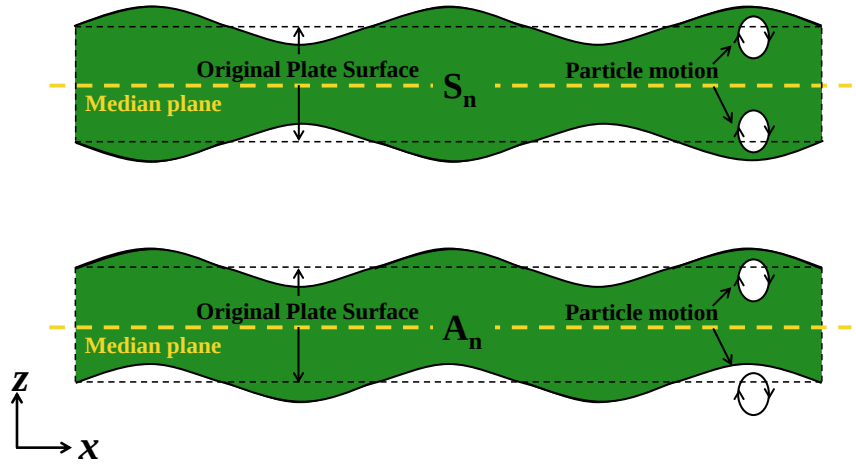

Figure 2-4. Schematic of symmetric and asymmetric Lamb wave modes.

2.3 Characteristics of Lamb Wave Modes in an AlN Film

2.3.1 Lamb Wave Modes

When surface acoustic waves are guided laterally into a sufficiently thin enough (h<) plate, they are referred to as Rayleigh-Lamb waves or Lamb wave [5]. Lamb wave modes generally only have displacements in the x and z directions, so depending on the symmetry of the particle displacements associated with the wave relative to the median plane of the plate, Lamb waves are sorted into symmetric and anti-symmetric modes, as illustrated in Figure 2-4.

Generally, the different plate modes are denoted as S_n or A_n, representing the nth order symmetric or asymmetric Lamb wave modes, where 'n' is an integer ranging from 0 to infinity and represents the number of standing waves along the plate thickness. Figure 2-5 shows the displacement fields of different Lamb wave modes from COMSOL. The fundamental symmetric mode is sometimes referred to as contour modes, and anti-symmetric modes sometimes referred to as flexural modes. For single AlN thin films, the high modes are difficult to be observed because of their smaller coupling coefficient compared to fundamental modes.

2.3.2 The Phase Velocity (v_p) of the Symmetric Fundamental (S_0) Mode

There are three fundamental boundary conditions (BCs) for AlN membranes: both surfaces free (open-circuited), one surface metallized (short-circuited) and the other free (open-circuited), and both surface metallized (short-circuited), as illustrated in Figure 2-6: BCs a, b and c. Here the mechanical effect of the metallization is ignored, in other words the metallization is assumed to be infinitely thin.

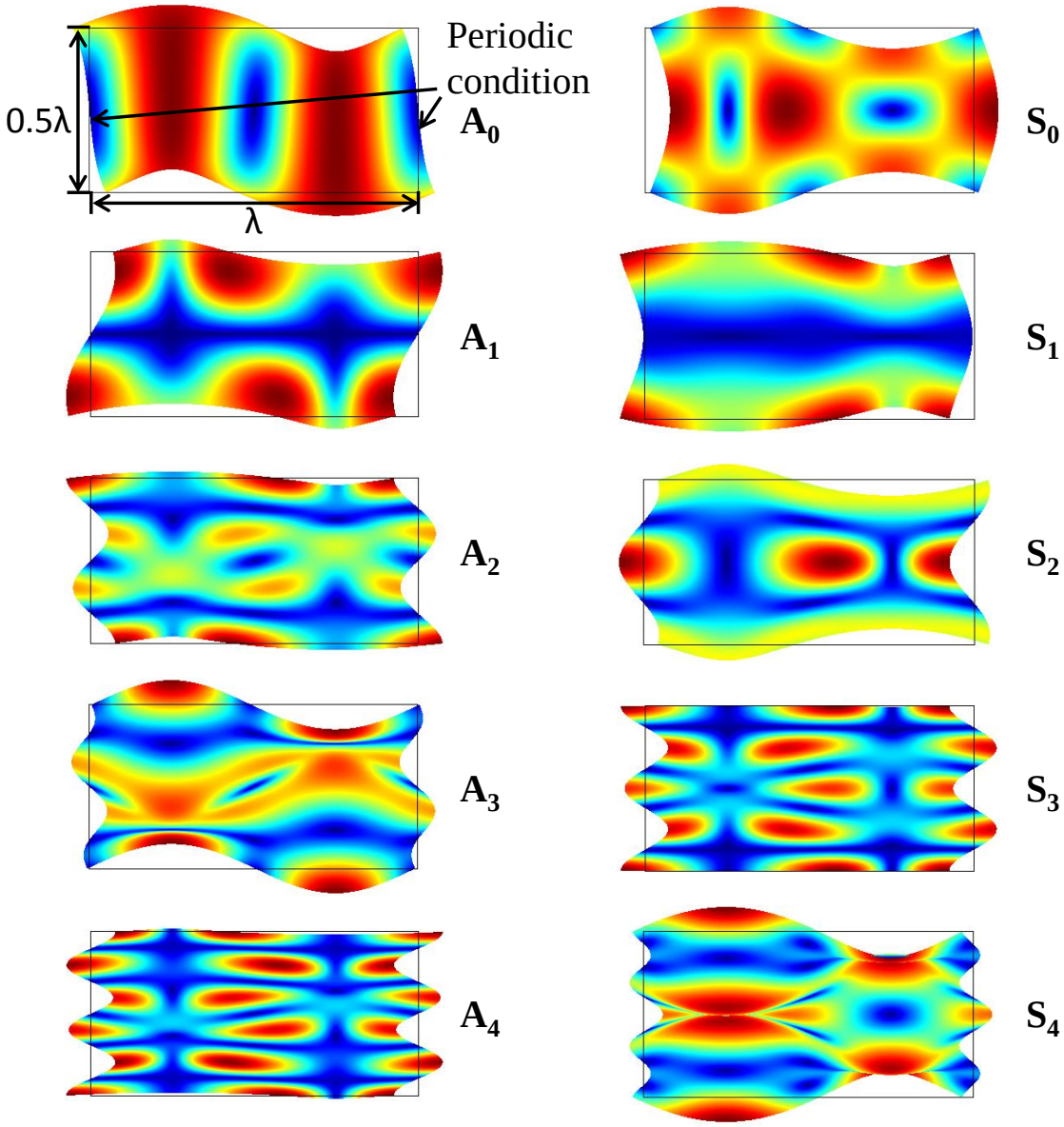

Figure 2-5. Displacement fields of different Lamb wave modes from FEA simulation.

The phase velocities of the symmetric fundamental (S_0) mode are computed for these three BCs based on the approach by Nassar [18] and using the material data for AlN shown in Table 2-2. The acoustic propagation properties are dispersive and are generally characterized by the normalized AlN thickness. The metallization slightly lowers the phase velocity, and the difference is actually determined by the electromechanical coupling coefficient (k^2), which will be introduced later. Otherwise, since the phase velocities of the three scenarios are very close, we will use the open-open phase velocity when discuss phase velocities for simplicity later in this report.

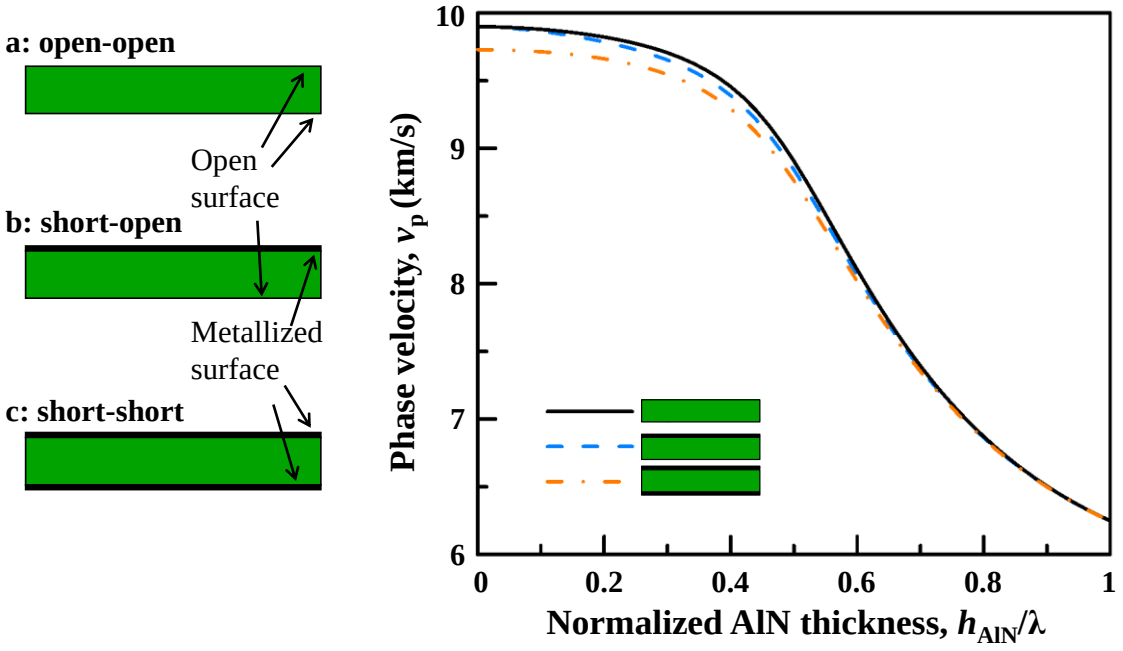

Figure 2-6. Dispersion of the phase velocity for the three basic boundary conditions for AlN Lamb wave devices using the lowest symmetric Lamb wave mode S_0.

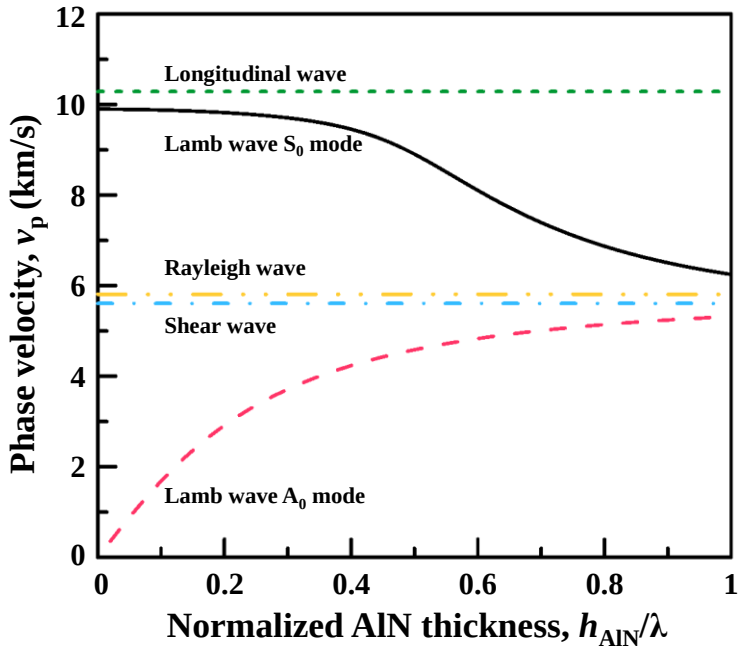

Figure 2-7. Calculated phase velocities of the first two Lamb wave modes comparing with the phase velocities of longitudinal, Rayleigh and shear waves propagating in an AlN membrane.

Fig. 2–7 shows the calculated phase velocity dispersions of the first two Lamb wave modes propagating in an AlN membrane, comparing with the phase velocities of

longitudinal, Rayleigh and shear waves in AlN. The S_0 Lamb wave mode shows a phase velocity near 10000 m/s which is close to the phase velocity of longitudinal wave (BAW), and it exhibits much weaker phase velocity dispersion than the A_0 Lamb wave mode. The high phase velocity of the S_0 mode in an AlN plate is suitable for high frequency devices and the weak phase velocity dispersion is preferred for fabrication robustness. When the plate is becoming thick, both the phase velocities of the A0 and S0 Lamb wave modes approaches that of Rayleigh mode.

2.3.3 The Electromechanical Coupling Coefficient (k^2) of the S_0 Mode

The electromechanical coupling coefficient of Lamb waves is estimated based on the difference of the phase velocities for a free surface v_o and metallized surface v_m, as

$$k^2 \cong \frac{v_o^2 - v_m^2}{v_o^2}. \tag{2.20}$$

This method of estimating k^2 is valid as long as the plate thickness h is smaller than the wavelength λ [23], which is the case for all computed results presented in this chapter. More complicated cases will be discussed next chapter involving the potential of electrodes using Finite Element Analysis (FEA). The coupling coefficients k^2 for the three configurations are based on the respective configurations for v_o and v_m illustrated for each of the cases in Figure 2-8 and calculated in Figure2-6. The results of the coupling for the three electrode configurations A, B and C are shown in Figure 2-9, with

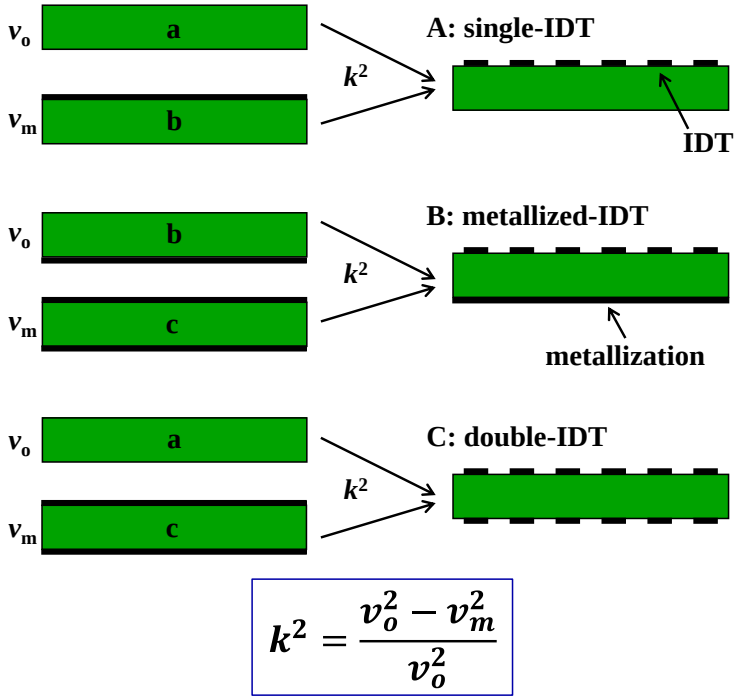

Figure 2-8. Three basic electrode configurations for Lamb wave devices: (a) single-IDT, (b) metallized-IDT, and (c) double-IDT.

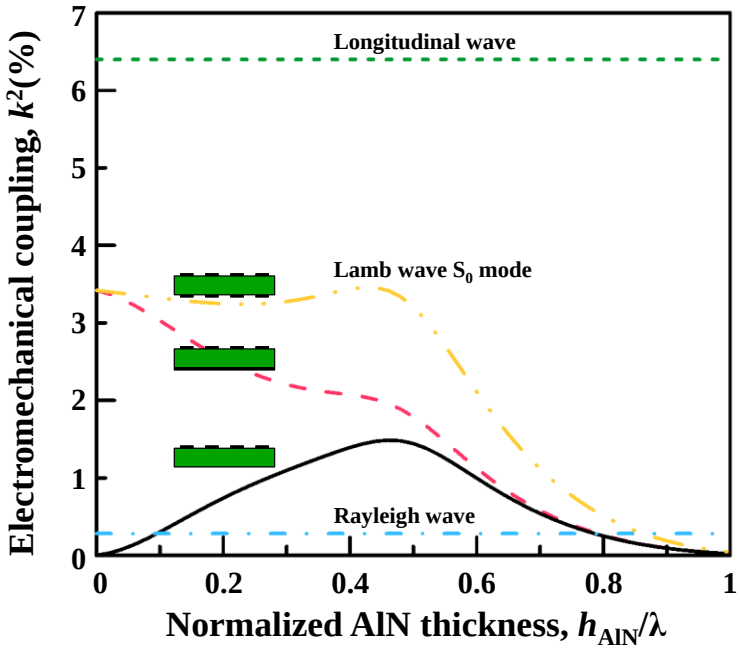

Figure 2-9. Comparison of the calculated k^2 of Lamb wave S0 mode with different electrode configurations and also the k^2 of longitudinal and Rayleigh waves.

comparison to longitudinal wave and Rayleigh wave.

Generally, double-IDT configuration exhibits the largest k^2 and single-IDT the smallest. Particularly, the single-IDT case has a peak k^2 when $\lambda \sim 0.5$ and is limited to 1.5%, the metallized-IDT electrode configuration enables k^2 as large as 3% when AlN is thin ($\lambda < 0.2$), and the double-IDT gives k^2 above 3% as long as $\lambda < 0.6$. However, the fabrication process for the double-IDT case is very complicated with an inclusion of CMP process in order to guarantee a smooth surface before AlN deposition and also a critical alignment between both IDTs. In contrast, the single-IDT case only needs a two-mask simple fabrication process.

2.3.4 The Temperature Coefficient of Frequency (*TCF*) of the S_0 Mode

Most materials become softer when temperature increases, meaning they have negative TCEs, including the AlN. This will lead to a decrease in frequency when temperature rises and an increase in frequency when temperature cools down. Table 4–2 lists the temperature coefficients of AlN which are used to predict the frequency-temperature behavior of the AlN LWR using the S_0 mode.

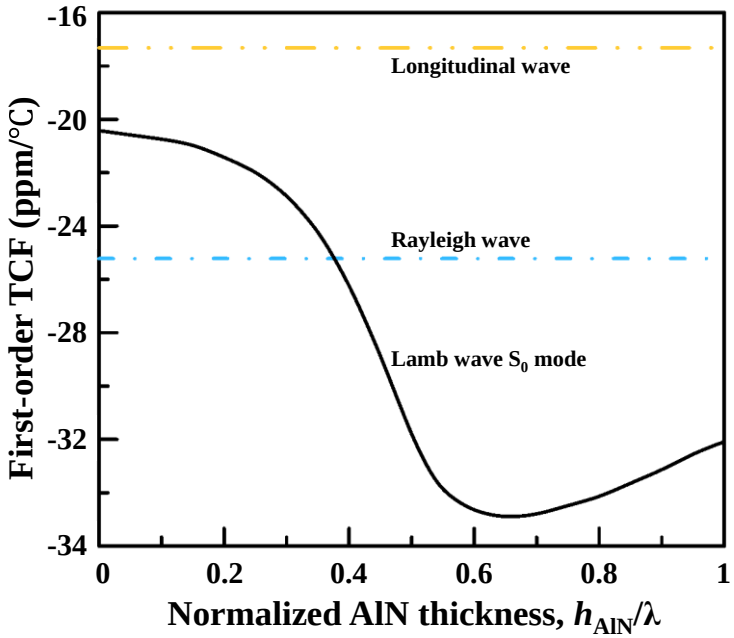

Figure 2-10. Calculated first-order TCFs of the Lamb wave S_0 modes comparing with longitudinal and Rayleigh waves in AlN.

The frequency drift of the AlN LWR not only dependent on the changes in the stiffness constants with temperature and but also the thermal expansion coefficients. Under linear approximation of the temperature dependence of the stiffness constants, the TCF of the AlN LWR is:

Table 2-3. Temperature coefficients of material constants of AlN used in the calculations. [50]

	Symbol	AlN	Units
Temperature coefficients of stiffness constants	TC_{11}	–37	(10^{-6} 1/°C)
	TC_{12}	–1.8	
	TC_{13}	–1.8	
	TC_{33}	–65	
	TC_{44}	–50	
	TC_{66}	–57	
Thermal expansion coefficients	α_{11}	5.27	(10^{-6} 1/°C)
	α_{33}	4.15	

$$TCF_{1st} = \frac{1}{v_p}\frac{\partial v_p}{\partial T} - \alpha_x$$

$$= \frac{1}{v_p}\frac{v_p(T_0+\Delta T)-v_p(T_0)}{\Delta T} - \alpha_x, \quad (2.21)$$

where $v_p(T_0)$ is calculated from the material constants in Table 2-3, and $v_p(T_0 + \Delta T)$ is calculated based on the new stiffness matrix $c_{ij}(T_0 + \Delta T)$:

$$c_{ij}(T_0 + \Delta T) = c_{ij}(T_0)(1 + TCE_{ij}). \quad (2.22)$$

The TCF of the AlN LWR can be theoretically predicted using the above formulas and the temperature dependence of material coefficients listed in Table 2–3. Since there are only first-order temperature coefficients of stiffness constants available in the literature [66], all theoretical calculations only considers the first-order effect on the TCF in this study. The calculated first-order TCFs of the Lamb wave S_0 modes comparing with longitudinal and Rayleigh waves in AlN are shown in Fig. 2–10. The AlN LWR using the S_0 mode shows a theoretical TCF range from -33 to –22 ppm/°C which is close to the experimental results [58]. What's more, it is interesting to note that the first-order TCF shows a dispersive characteristic and reaches the worst case when the AlN membrane thickness is around 0.62λ.

Chapter 3

Design of AlN Lamb Wave Resonators Utilizing S_0 Mode

3.1 Equivalent Circuit and Typical Frequency Response

As illustrated in Figure 3-1, a Lamb wave resonator usually consists of the AlN plate as the resonant cavity, the supporting tethers providing the rigid attachment to the substrate, and the IDT transducer that is two sets of electrodes connected alternatively to two bus bars placed on a piezoelectric substrate. The space *p* between two adjacent electrode fingers and their overlap length W are called pitch and aperture. The metallization ratio (η) is usually 0.5 and the IDT finger width is equal to quarter wavelength ($\lambda/4$) in this case. The resonance frequency is equal to the ratio of the phase velocity of the wave mode and the wavelength, thus determined by the wave characteristics and the IDT width:

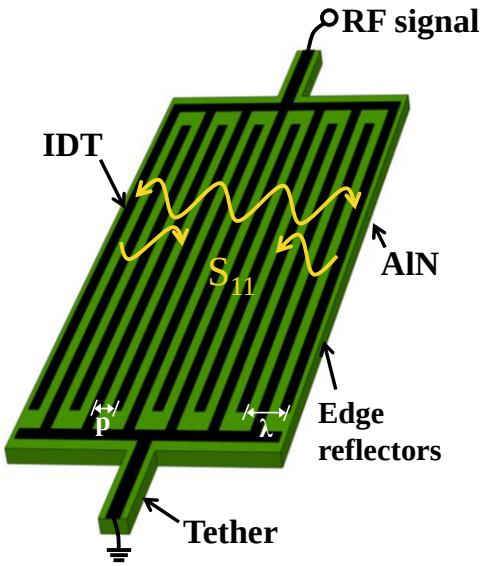

Figure 3-1. Illustration of one-port AlN Lamb wave resonator employing the edge-type reflector.

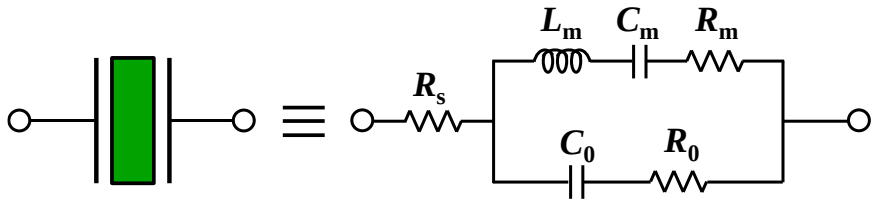

Figure 3-2. Modified Butterworth-Van Dyke (MBVD) equivalent circuit model

$$f_s = \frac{v_p}{\lambda} = \frac{v_p}{2p}. \tag{3.1}$$

A piezoelectric resonator usually can be described using the Butterworth-Van Dyke (BVD) equivalent circuit which consists of a mechanical resonance branch including a motional resistance (R_m), a motional capacitance (C_m), and a motional inductance (L_m) in series and a static capacitance (C_0) in parallel, as depicted in Figure 3-2. The static capacitance C_0 is simply formed by the capacitance between the IDT finger electrodes and the plate capacitance sandwiched between the top and bottom electrodes. As shown in Fig. 3-2, a modified Butterworth-Van Dyke (MBVD) equivalent circuit model including two loss resistors, R_s and R_0, was proposed to improve matching for real piezoelectric BAW resonators [**Error! Reference source not found.**]. Nominally, the eries resistor R_s describes the resistance of routing pads and electrodes, and the parallel resistor R_0 represents the parasitic resistance in the Si substrate [**Error! Reference ource not found.**]. Based on the six parameters in the MBVD equivalent circuit, the series and parallel resonance frequencies, f_s and f_p, the impedance $Z(\omega)$, and the quality factors at the series and parallel frequencies, Q_s and Q_p, can be expressed as [**Error! eference source not found.**], [**Error! Reference source not found.**]

$$f_s = \frac{\omega_s}{2\pi} = \frac{1}{2\pi}\sqrt{\frac{1}{L_m C_m}}, \tag{3.2}$$

$$f_p = \frac{\omega_p}{2\pi} = \frac{1}{2\pi}\sqrt{\frac{1}{L_m C_m}\left(1+\frac{C_m}{C_0}\right)}, \tag{3.3}$$

$$Z(\omega) = R_s + \frac{\left(R_0 + \frac{1}{j\omega C_0}\right)\left(R_m + \frac{1}{j\omega C_m} + j\omega L_m\right)}{R_0 + \frac{1}{j\omega C_0} + R_m + \frac{1}{j\omega C_m} + j\omega L_m}, \tag{3.4}$$

$$Q_s = \frac{1}{\omega_s (R_m + R_s) C_m}, \tag{3.5}$$

$$Q_p = \frac{1}{\omega_p (R_m + R_0) C_m}, \tag{3.6}$$

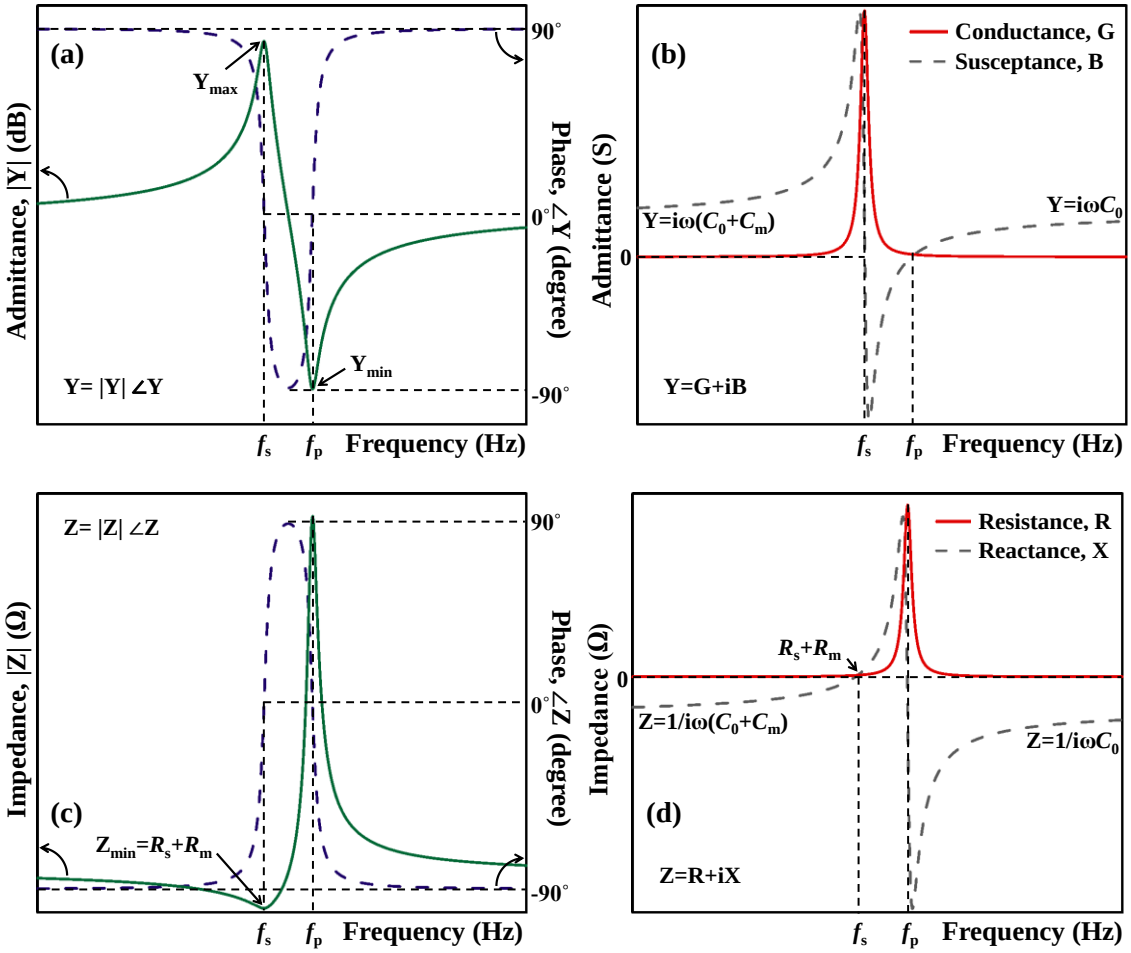

Figure 3-3. Typical frequency responses of a Lamb wave resnator.

where ω_s and ω_p are the angular frequencies at the series and parallel resonance frequencies, respectively. It should be noted that the expressions of the Q_s and Q_p are loaded quality factors at f_s and f_p, respectively, since the parasitic R_s and R_0 are included and hence lower the intrinsic mechanical quality factors.

Figure 3-3 presents the typical frequency response of a resonator with associated MBVD parameters. At resonance the spectrum shows the maximum admittance and a 0 degree phase, and at anti-resonance it exhibits the minimum admittance and a 0 degree phase. The real part of admittance (conductance) is near 0 at frequencies off resonance and the imaginary part (susceptance) is highly dependent on the static capacitance. The opposite can be observed for the impedance spectrum of the frequency response.

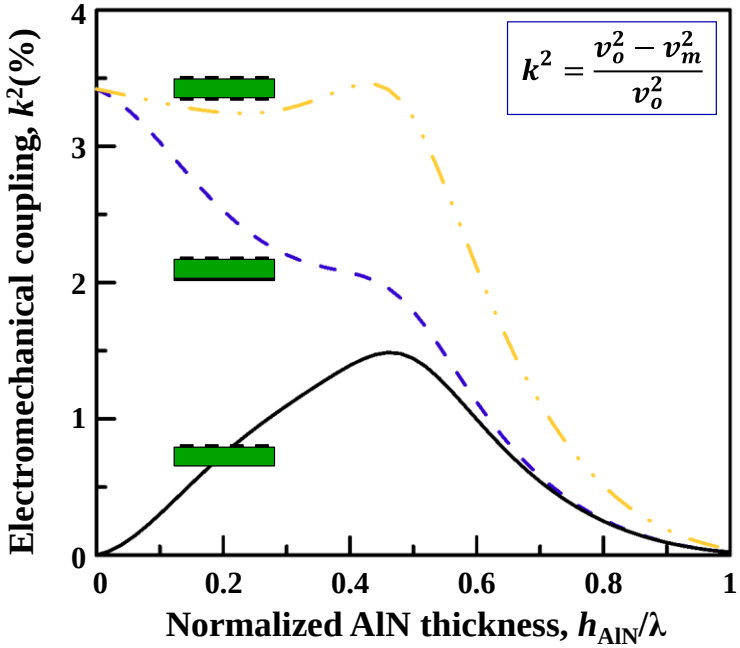

Figure 3-4. Numerically calculated electromechanical coupling coefficients for three metallization conditions: single-IDT, metalized-IDT, and double-IDT.

3.2 The Effective Coupling Coefficient (k^2_{eff}) Optimization

3.2.1 Electrode Configuration and AlN thicknesses

As introduced in the previous chapter, the intrinsic electromechanical coupling coefficient k^2 is a measure of the energy transduction efficiency between the electrical and mechanical domains, and can be calculated by the velocity difference equation. Nevertheless, the effective electromechanical coupling coefficient (k_{eff}^2) for resonator devices from the measured results can be evaluated in several ways, among which the most often used definitions is IEEE standard definition.

$$k_{eff}^2 = \frac{\pi}{2}\frac{f_s}{f_p}[\tan(\frac{\pi}{2}\frac{f_s}{f_p})]^{-1}. \quad (3.7)$$

The most used approximation for the effective coupling coefficient is

$$k_{eff}^2 = \frac{\pi^2}{4}(\frac{f_p - f_s}{f_p}). \quad (3.8)$$

The k_{eff}^2 is in fully consistent with the k^2 for BAW resonators by this definition. But for Lamb wave resonators there are small difference between these two measures. What's

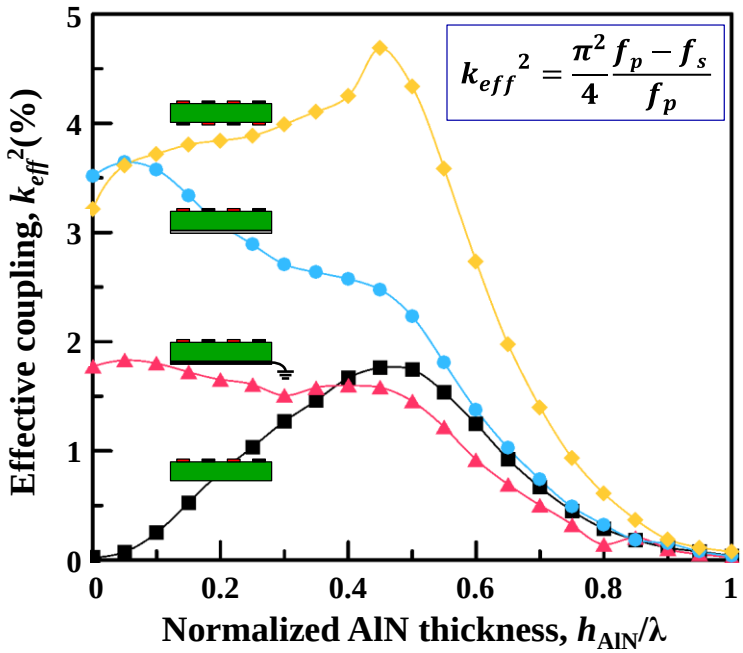

Figure 3-5. Simulated effective coupling of the Lamb wave S_0 mode using COMSOL for four electrode configurations: single-IDT, with a grounded bottom electrode, with a floating electrode, and double-IDT.

more, although different metallization configurations are considered for the k^2 as shown in Figure 3-4, the difference between grounded and floating bottom electrode should be considered for the k_{eff}^2 from the device perspective, shown in Figure 3-5. The comparison between Figure 3-4 and Figure 3-5 reveals that the IDT-metallization case for the calculation of k^2 corresponds to the floating bottom electrode case for the simulation of k_{eff}^2, and the difference between the corresponding k^2 and k_{eff}^2 are within 10%.

3.2.2 Electrode Material Selection

Except for the effects on the quality of the AlN thin films grown on the metallized bottom surface, there are two main concerns of the bottom metallization which strongly affect the performance of the AlN LWR: phase velocity and electromechanical coupling strength. As shown in Table 4–1, most of metal materials usually have a low acoustic velocity so the phase velocity of the S_0 Lamb wave mode is decreased by the bottom metallization. Figure 3–6 illustrates the mass loading effect of various metals on the phase velocity of the S_0 Lamb wave mode for a normalized metal thickness (h_{metal}/λ) fixed to 0.02. Generally the material with larger mass density decreases the phase velocity more.

As presented in Fig. 3–7, the electromechanical coupling coefficient would be enhanced by the IDT metallization. Generally, the materials with larger acoustic impedance increase the k^2 more than the low-ρv_p materials, so W, Pt are good candidate

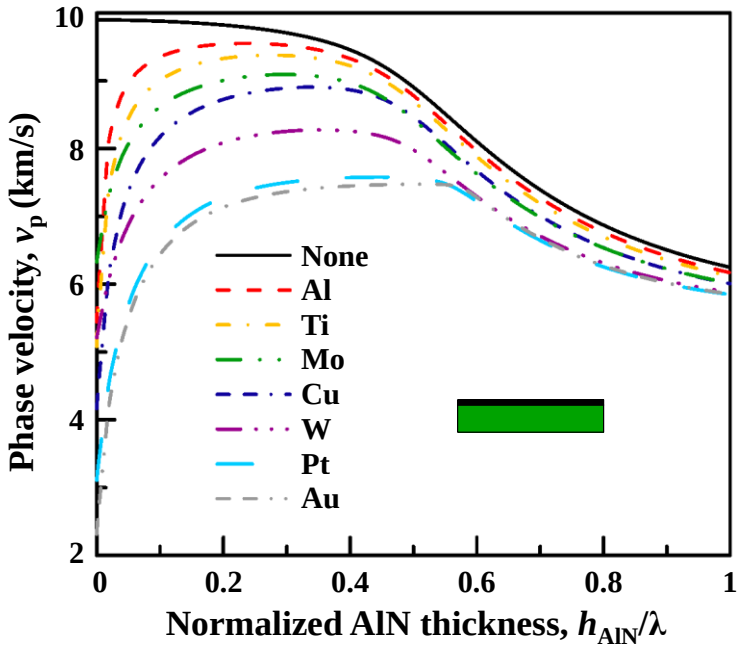

Figure 3-6. Calculated phase velocities of the S_0 mode in the AlN films with various bottom metals while the metal thicknesses normalized to the wavelength are fixed to 0.02.

for the IDT metal material. However, W has a large electrical resistivity and large roughness, Pt is the better metal choices for the IDT metallization.

3.4 Temperature Compensation Technique

Table 3-1. Material properties of selected metals [28], [39].

	Al	Ti	Mo	Cu	W	Pt	Au	Units
Density	2700	4500	10200	8960	19250	21400	19300	(kg/m^3)
C_{11}	111.3	166	462.1	210.6	590	374	220.2	(10^9 N/m^2)
C_{12}	59.1	92	157.7	107.8	200	251	160.4	(10^9 N/m^2)
C_{44}	26.1	44	108.9	51.4	135	76.5	29.9	(10^9 N/m^2)
Resistivity	2.8	42	5.7	1.68	5.39	10.7	2.214	(10^{-6} Ω·cm)
Thermal expansion	18	8.6	5.1	16.5	4.3	8.9	14.2	(10^{-6}/℃)

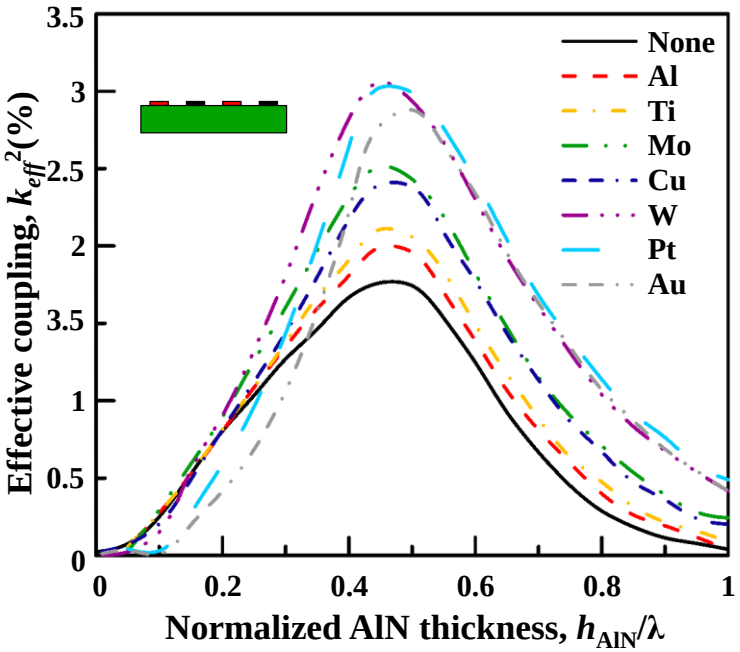

Figure 3-7. Simulated k^2 of the S_0 mode in the AlN thin films with various bottom metals while the metal thicknesses normalized to the wavelength are fixed to 0.02.

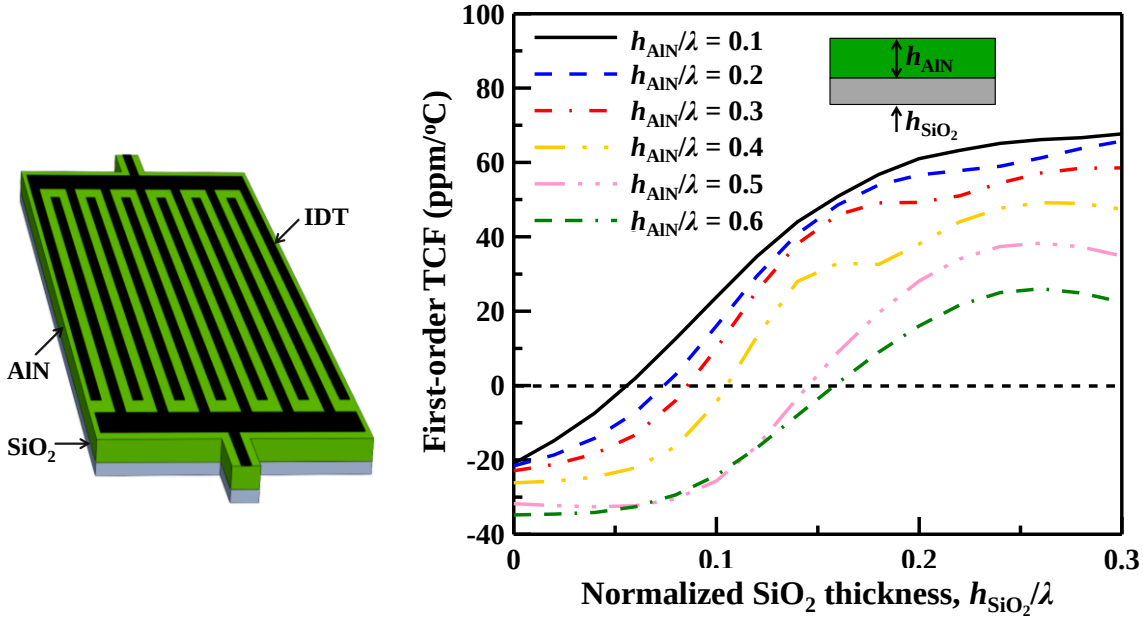

Figure 3-8. Illustration of the temperature compensated AlN/SiO_2 Lamb wave resonator and the calculated first-order TCFs for different AlN and SiO_2 thicknesses

Unlike quartz-based devices offering a variety of specific temperature compensation cuts for the bulk and surface acoustic waves, AlN exhibits the negative TCE, making it

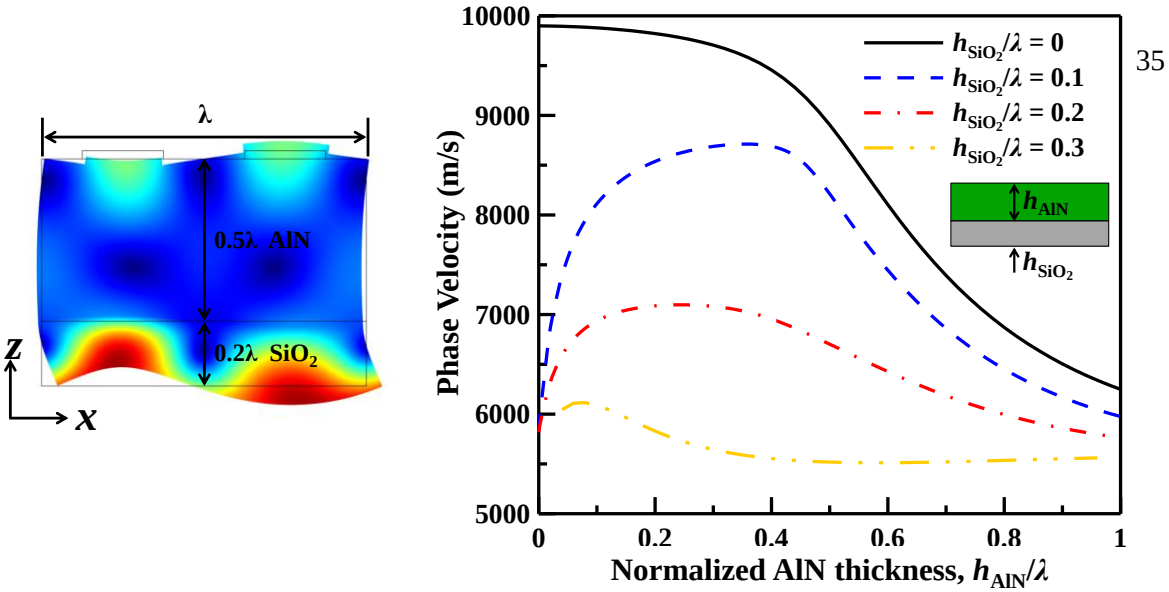

Figure 3-9. Calculated phase velocities of the Lamb wave S_0 modes for different AlN and SiO2 thicknesses.

impossible to enable intrinsically temperature-compensated electroacoustic devices. The temperature compensation of the AlN-based devices is therefore achieved by employing thin film materials with opposite TCF. By adding a SiO_2 layer with a TCF of 85 ppm/°C onto the piezoelectric AlN layer, a robust temperature compensation approach for the LWRs on an AlN/SiO_2 bilayer plate has been successfully demonstrated at room temperature and high temperatures.

Unfortunately, as is shown in Figure 3-9, the low elastic constants and non-

Table 3-2. Material constants of AlN and SiO_2 used in the calculations. [50]

	Symbol	AlN	SiO_2	Units
Stiffness constants	C_{11}	345	78.5	(10^9 N/m^2)
	C_{12}	125	16.1	
	C_{13}	120	16.1	
	C_{33}	395	78.5	
	C_{44}	118	31.2	
	C_{66}	110	31.2	
Mass density	ρ	3260	2210	(kg/m^3)
Piezoelectric constants	e_{15}	–0.48	–	(C/m^2)
	e_{31}	–0.58	–	
	e_{33}	1.55	–	
Dielectric constants	ε_{11}	8.0	3.32	(10^{-11} F/m)
	ε_{33}	9.5	3.32	

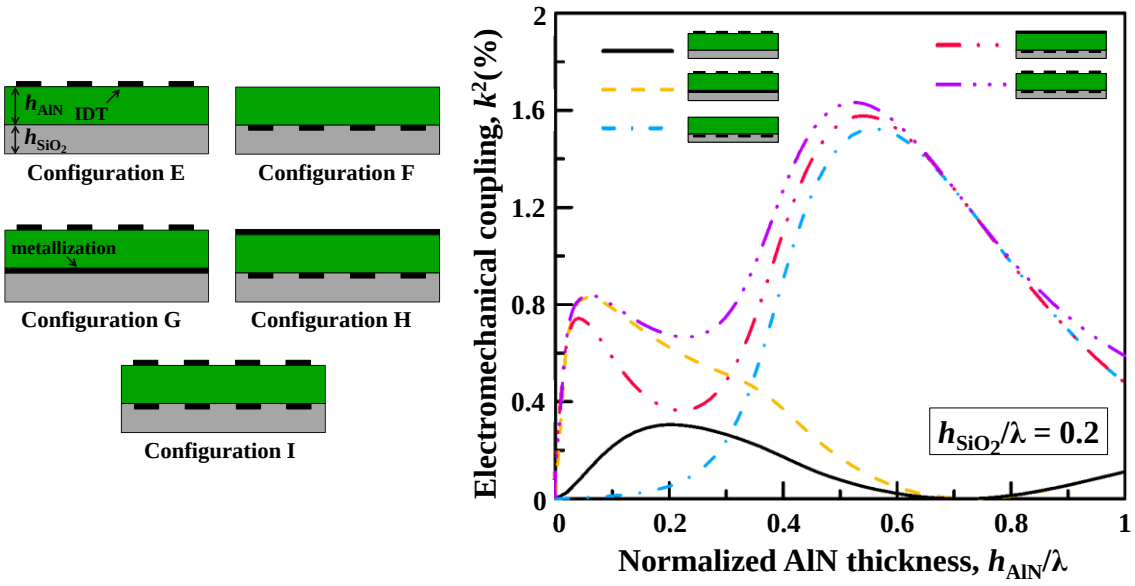

Figure 3-10. Calculated electromechanical coupling coefficients of the QS_0 mode for different electrode configurations listed when h_{SiO_2}/λ=0.2.

piezoelectricity of the SiO_2 layer causes substantial reductions in the phase velocity and electromechanical coupling coefficient. Furthermore, the asymmetrical composite plate traps less acoustic waves in the AlN active layer so that the piezoelectric energy is excited less efficiently to enable lower v_p and smaller k^2 for the S_0 Lamb wave mode in the AlN/SiO_2 membrane. Figure 3-9 also shows the phase velocities for different AlN and SiO_2 thicknesses calculated using the material parameters listed in Figure 4-2. It is very clear that the adding layer of SiO_2 substantially lowers the phase velocity. When the normalized SiO_2 thickness reached 0.3, the phase velocity of the structure is almost halved compared to the pure AlN membrane.

Because of the asymmetry in the z-axis direction, five different electrode configurations should be considered for the analysis of electromechanical coupling, as is listed in Figure 3-10, and the calculated electromechanical coupling from the material properties in Table 3-2 for a mostly used SiO_2 thickness - 0.2 - is also given in the figure. It is obvious that the double-IDT configuration always exhibit the largest coupling, the configurations when the IDTs are placed in the outer surface of AlN shows a larger coupling when the normalized AlN thickness is around 0.55, and the configurations when the IDTs are placed in the interface of AlN and SiO_2 shows a larger coupling when the normalized AlN thickness is around 0.05.

Figure 3-11 also compares the electromechanical coupling for different electrode configurations but at fixed normalized AlN thicknesses, which indicate that for thin AlN the bottom electrode is highly preferred and for thick AlN placing the IDT at the interface can largely increase the k^2.

Furthermore, the trade-off between the TCF and k^2 can be observed in the same propagation medium. As shown in Figure 3-12, when the k^2 on the AlN/SiO_2 composite membrane achieve a locally minimum, it exhibits a locally maximal TCF, and vice versa,

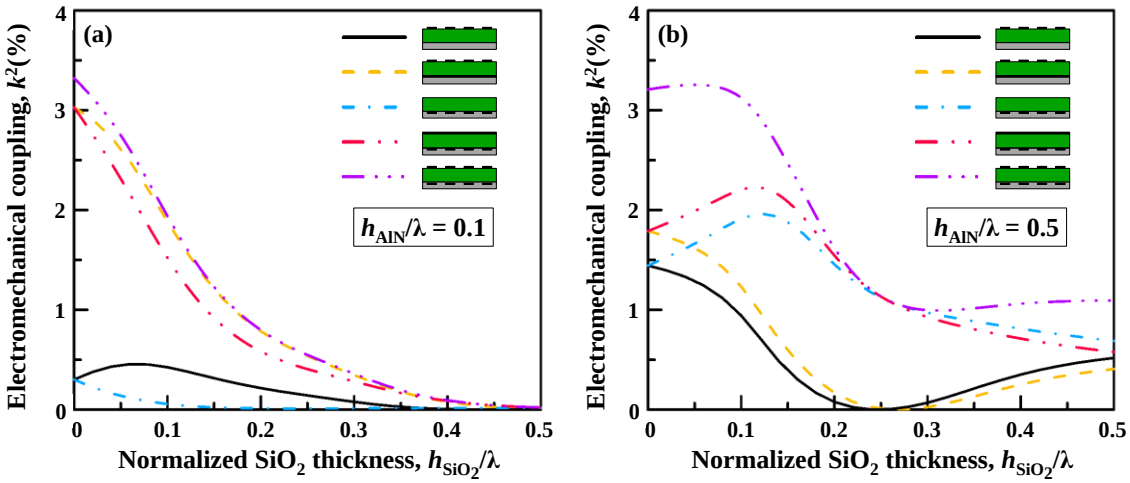

Figure 3-11. Calculated electromechanincal coupling coefficients for different electrode configurations at fixed normalized AlN thicknesses.

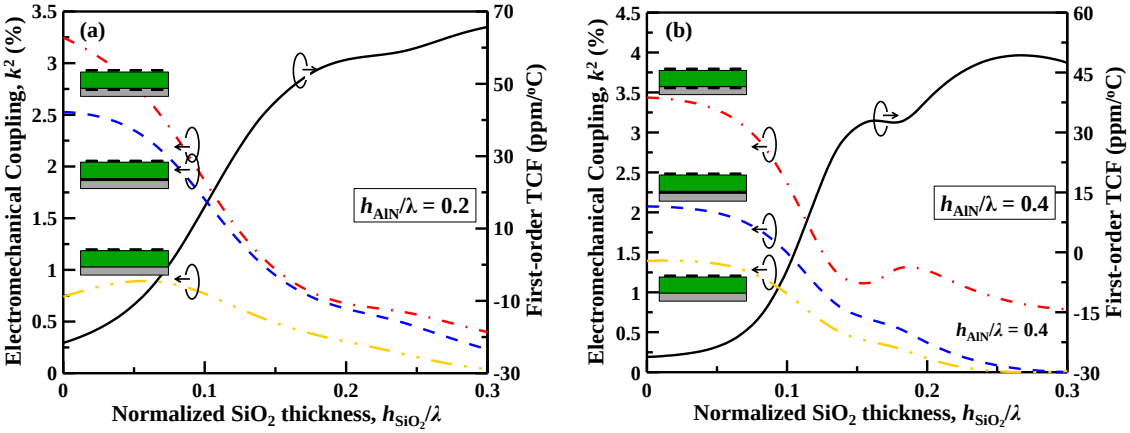

Figure 3-12. Trade-off between the first-order TCF and intrinsic k^2 of the QS_0 mode in the AlN/SiO_2 bilayer when h_{AlN}/λ = 0.2 and h_{AlN}/λ = 0.4.

revealing the trade-off between the TCF and k^2 in the piezoelectric LWRs.

The above discussions indicate that a correct transducer configuration with proper selections of the AlN and SiO_2 thicknesses enables the $SiO_2/AlN/SiO_2$ LWRs to have high phase velocity, large intrinsic electromechanical coupling coefficient, and good temperature-frequency stability at high temperatures.

3.5 Microfabrication Process

The microfabrication process used for making the devices is a two-mask process, as shown in Figure 3-13. A 300-nm-thick low-stress nitride (LSN) layer for electrical

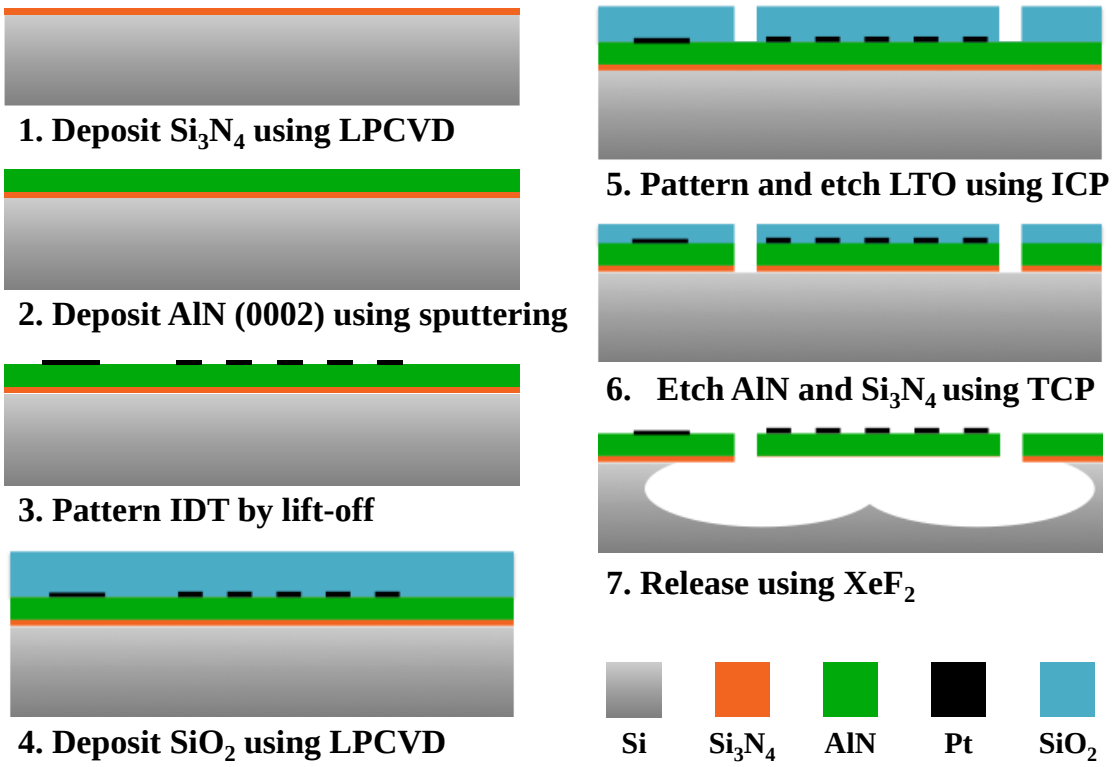

Figure 3-13. Cross-sectional process flow of the single-IDT AlN LWRs.

isolation was first deposited on the high-resistivity silicon (100) wafer. A highly *c*-axis oriented AlN film with a full width at half maximum (FWHM) value of rocking curve measurement equal to 1.33° was deposited onto the LSN layer by magnetron reactive sputtering. A 180-nm-thick platinum (Pt) IDT electrodes layer with a 20-nm-thick chromium (Cr) adhesion layer was sputtered on the AlN thin film and patterned using a lift-off process. A low temperature oxide (LTO) hard mask layer was deposited at around 400°C and patterned by C_4F_8-based dry etching. The AlN thin film was then patterned by the Cl_2-based etching, followed by a CF_4-based reactive ion etching (RIE) process to remove the remaining LTO layer. The AlN Lamb wave resonators were finally released using XeF_2-based isotropic dry etching of the Si substrate, and the thin LSN layer beneath the AlN layer was simultaneously removed by XeF_2.

Fig. 3-14 (a) shows the SEM images of the resonators on the 4-μm-thick AlN membranes and Figure 3-14 (b) presents the released air cavity.

The electromechanical coupling strength and quality factor is strong correlated to the crystalline orientation of the AlN, so the deposition of highly *c*-axis oriented AlN thin films is the most critical process for piezoelectric devices. The correlation between k_2 and AlN grain orientation has been found and suggests that maximum coupling can be achieved if the rocking curve FWHM value of the AlN film is below 2° [104]. Except for the crystalline orientation, a low residual stress is equally important since the released devices might break due to a high residual stress. In this work, the AlN thin film was deposited on various substrates by AC (40 kHz) powered S-Gun magnetron. Prior to the

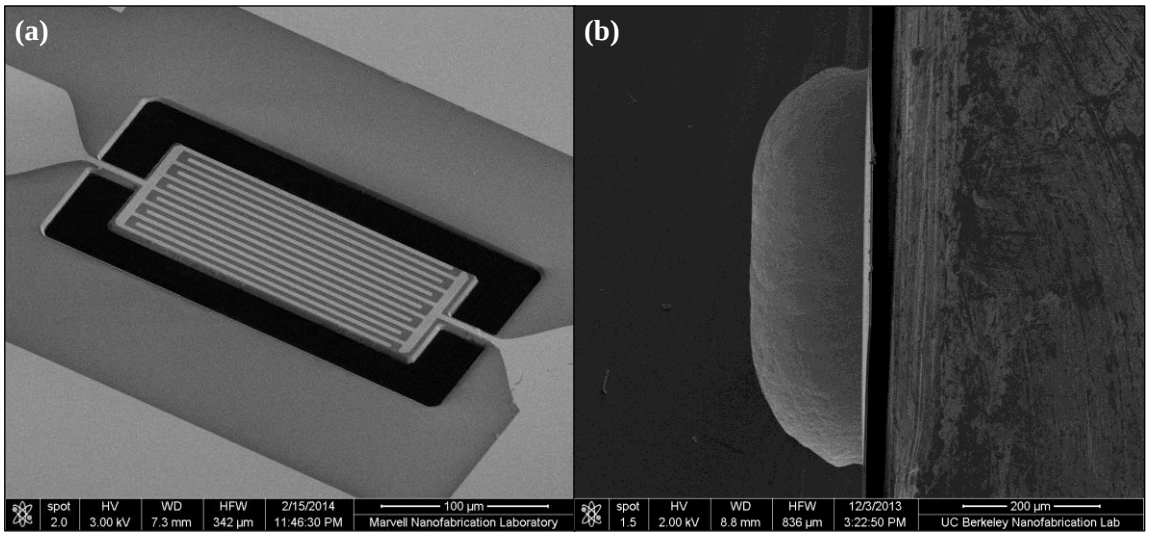

Figure 3-14. SEM image of the fabricated Lamb wave resonator and the air cavity structure.

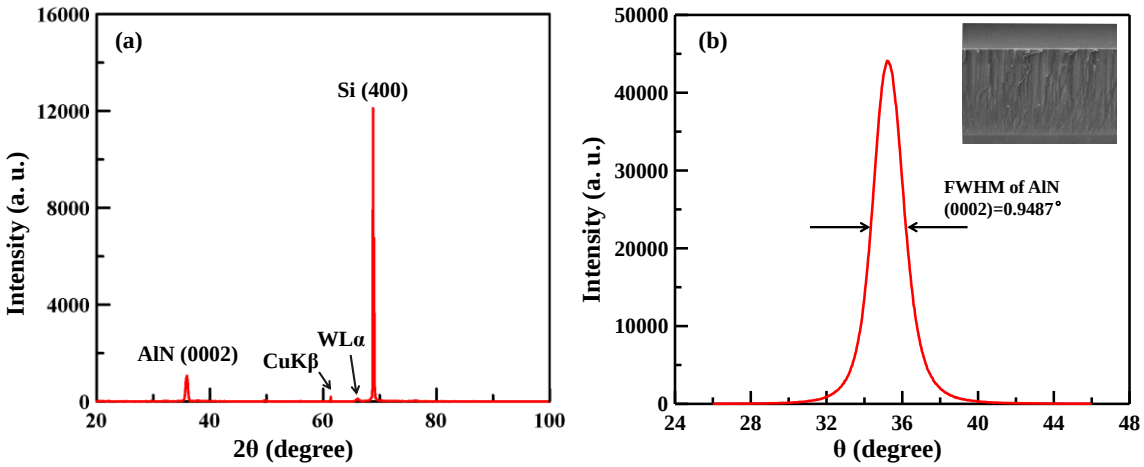

Figure 3-15. XRD (a) normal-couple scan and (b) rocking curve measurement of 4-µm thick AlN thin film deposited with nearly zero stress.

AlN film deposition, the surface of the substrate was pretreated by RF plasma etching to achieve smooth surface roughness.

In Figure 3-15 a typical normal coupled scan and a rocking curve scan of an AlN thin film deposited on a silicon nitride substrate are shown. The diffraction pattern from a highly c-axis oriented AlN thin film shows a peak at $2\theta = 36.4°$ in the normal coupled scan, and a minimum FWHM value of the 0002 rocking curve centered at ω=18.2°. These crystalline characterizations are done using a Siemens D5000 X-ray Diffractometer.

Chapter 4

Q Enhancement of AlN Lamb Wave Resonators Using Butterfly-shaped Plates

The small-in-size and CMOS-compatible MEMS resonators are likely to be the driving core of a new generation of electronic devices such as RF filters, sensors, and timing references [51], [52]. Thanks to the high frequencies, low R_m, and capability of multiple frequencies operation on a single chip, the AlN Lamb wave resonators utilizing the S_0 mode have attracted attention among various micromechanical resonator technologies [53]–[57]. However, the AlN Lamb wave resonator usually shows a Q below 2,000 due to complicated energy dissipation mechanisms, so an improvement in its Q is highly desirable to further enable low-loss filters, high-sensitivity sensors, and low-phase-noise oscillators.

3.1 Loss Mechanisms

Unlike the capacitive resonators that tend to show a very high Q but a huge R_m, piezoelectric resonators usually exhibit a large coupling which leads a small Rm, but unfortunately they show a medium Q [52], [58], [59]. Different loss mechanisms in piezoelectric MEMS resonators have been investigated recently, and the interfacial loss, causing from the stress jump at the material interface [62]–[64] as well as the anchor loss, representing the acoustic energy leakage via the support tethers into the substrates [64]–[71], are now suspected of the primary energy dissipation mechanisms. Fortunately, the electrode-to-piezoelectric stress can be minimized with the optimized metal deposition conditions [56] or separating the piezoelectric layer from its metal electrode [63] to reduce the interfacial loss. By suppressing the acoustic wave leakage through the tethers, the Q of the piezoelectric resonators can be improved [66]–[71].

Generally, the anchor loss of the MEMS resonators can be minimized by many strategies, such as positioning the tethers at nodal locations of the resonance mode, narrowing the width of the support tethers, using different materials for the support and

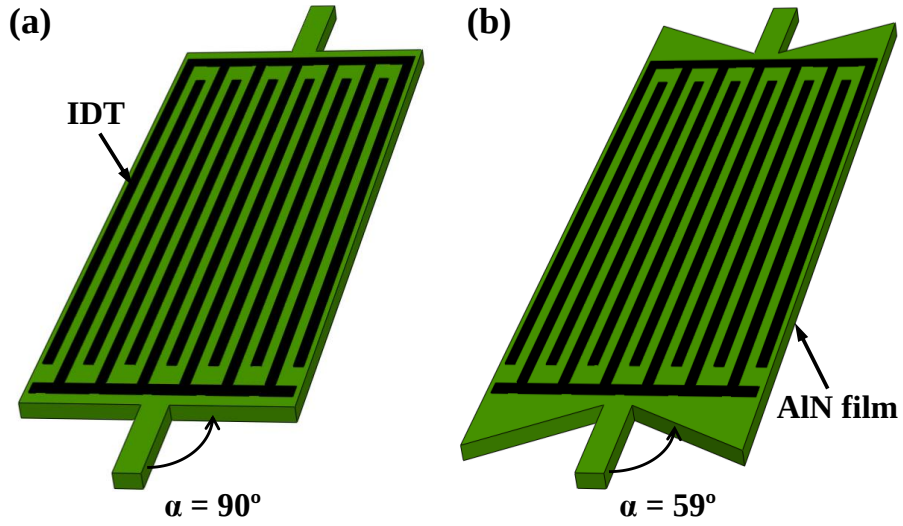

Figure 4-1. Illustration of (a) a conventional AlN Lamb wave resonator employing a rectangular plate with tether-to-plate angle α = 90º, and (b) an AlN Lamb wave resonator with a butterfly-shaped plate with α = 59º.

vibrating body to form an acoustic impedance mismatch, and designing the tether length with an odd multiple of a quarter-wavelength (λ/4) [65]. Another effective way of reducing the anchor loss is to reflect the acoustic waves leaky via the tethers back to the resonant structure [67], [70], [71] or to concentrate the acoustic wave displacement far from the supporting area [18]. Recently, the suspended biconvex edges were demonstrated to efficiently concentrate the Lamb wave distributions in the resonance plate and then boost the *Q*. However, some unwanted spurious vibration modes were also introduced due to the curved reflecting edges [68].

To effectively reduce the anchor loss without introducing unwanted spurious modes, for the first time, a novel AlN Lamb wave resonator utilizing a butterfly-shaped plate is investigated to enhance the anchor *Q* in this work. Fig. 1(a) illustrates a conventional AlN Lamb wave resonator based on a rectangular thin plate consisting of one interdigital transducer (IDT) and two suspended free edges. As shown in Fig. 1(b), another AlN α = 90º α = 59º.a rectangular plate with tether-to-plate angle α = 90º, and (b) an AlN Lamb wave resonator with a butterfly-shaped plate with α = 59º. Lamb wave resonator composed of the same IDT electrode configuration and free-edge reflector, but the butterfly-shaped plates with a tether-to-plate angle α = 59º is employed as the vibrating structure.

3.2 Resonator Design and Finite Element Analysis

As is well known, the mechanical *Q* describes how under-damped a resonator is and can be generally expressed as:

$$Q = 2\pi \times \frac{E_{\text{stored}}}{E_{\text{dissipated}}}, \tag{4.1}$$

where E_{stored} is the vibration energy stored in the resonator and $E_{\text{dissipated}}$ denotes the energy dissipated per cycle of vibration, respectively. It is clear that to obtain a higher Q, it requires more energy stored in the resonator and less energy dissipation, indicating that the magnitude of Q ultimately depends on the energy loss in resonators. The most relevant loss mechanisms in piezoelectric resonators are the anchor loss, interface loss, thermoelastic damping (TED), material damping, and other unknown losses 60, 61. Then, the total Q can be estimated by adding the impact of each specific energy loss mechanism:

$$\frac{1}{Q_{\text{total}}} = \frac{1}{Q_{\text{anchor}}} + \frac{1}{Q_{\text{interface}}} + \frac{1}{Q_{\text{TED}}} + \frac{1}{Q_{\text{material}}} + \frac{1}{Q_{\text{unknown}}}. \tag{4.2}$$

The interface loss, $Q_{\text{interface}}$, is caused by the plane stress jump at the material interface and can be minimized by controlling the interfacial stresses during the deposition process. The thermoelastic damping, Q_{TED}, means the energy dissipation during vibration which produces a strain gradient, which leads to a temperature gradient, yielding the heat flow as well as the energy loss. The material damping, Q_{material}, is related to the crystal defects in the material, surface roughness, or grain size so it is difficult to estimate the Q_{material}. In this work, we simply assume that the anchor loss, Q_{anchor}, is the main energy dissipation source in the resonator so we simplify the Q_{total} is contributed by the Q_{anchor} and other losses, Q_{other}, as following:

$$\frac{1}{Q_{\text{total}}} = \frac{1}{Q_{\text{anchor}}} + \frac{1}{Q_{\text{other}}}. \tag{4.3}$$

In this work, we propose a novel AlN plate geometry to reduce the tether vibration caused by the resonant structure to increase the Q_{anchor}. In order to study the effect of the plate shape on Q, the Lamb wave resonators on AlN plates utilizing a rectangular plate and a butterfly-shaped plate are designed and compared as summarized and listed in

Table 4-1: Geometric dimensions of the AlN Lamb wave resonators.

	Conventional	**Butterfly-shaped**
IDT finger electrode	13	13
IDT aperture	180 μm	180 μm
IDT electrode width	3 μm	3 μm
IDT electrode thickness	200 nm	200 nm
Tether-to-plate angle	90°	59°
Tether length	33 μm	33 μm
Tether width	8 μm	8 μm
AlN plate length	210 μm	252 μm
AlN plate width	78 μm	78 μm
AlN plate thickness	4.0 μm	4.0 μm

Table 4-1.

Recently, a new finite element analysis (FEA) simulation approach which is based on the perfectly matched layer (PML) technique is introduced to evaluate Q_{anchor} in MEMS resonators 70–72. The PML can rapidly attenuate the acoustic waves leaky via the support tethers and also perfectly match the rest of the domain so there is no spurious reflection caused by the substrate/PML interface as shown in Fig. 2. Herein, we employ the PML-based FEA approach and the commercially available FEA software, COMSOL Multiphysics®, to analyze the Q_{anchor} of two resonators using different plate geometries. The Q_{anchor} can be obtained by using the equation 64, 70–72:

$$Q_{anchor} = \frac{\mathrm{Re}(\omega)}{2\,\mathrm{Im}(\omega)}, \tag{4.4}$$

where ω is the eigen-frequency of the desired mode solved in the FEA model.

Fig. 2 illustrates the FEA model of half an AlN plate with one simple beam tether attaching to the semi-cylinder substrate plate which is covered by the PML to assume the substrate is a semi-infinite plate. The radius of the substrate plate is set as 2λ while the radius of the PML equals 4λ (i.e., the PML thickness is equal to 2λ). The mesh adopted in the FEA model is also shown in Figure 4-2. A symmetric boundary condition is applied to the center face of the AlN plate to ensure the eigen modes are solved for a whole plate.

Figure 4-3 (a) presents the mode shape (displacement profiles) of the S_0 Lamb wave at resonance in the conventional rectangular AlN plate. There is obvious displacement in the support tether, indicating a part of mechanical energy would lose via the tether

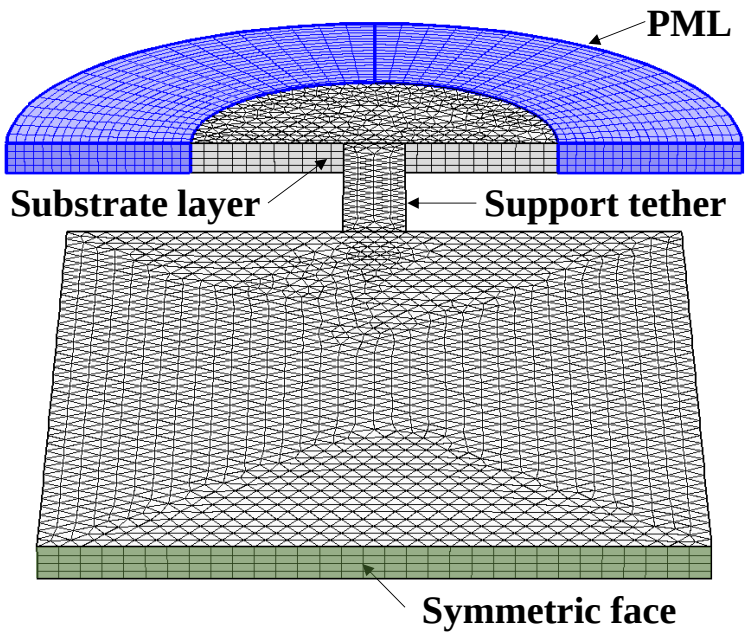

Figure 4-2. Illustrations of half an AlN plate with a simple beam tether attaching to a substrate layer covered by PMLs and the mesh adopted in FEA.

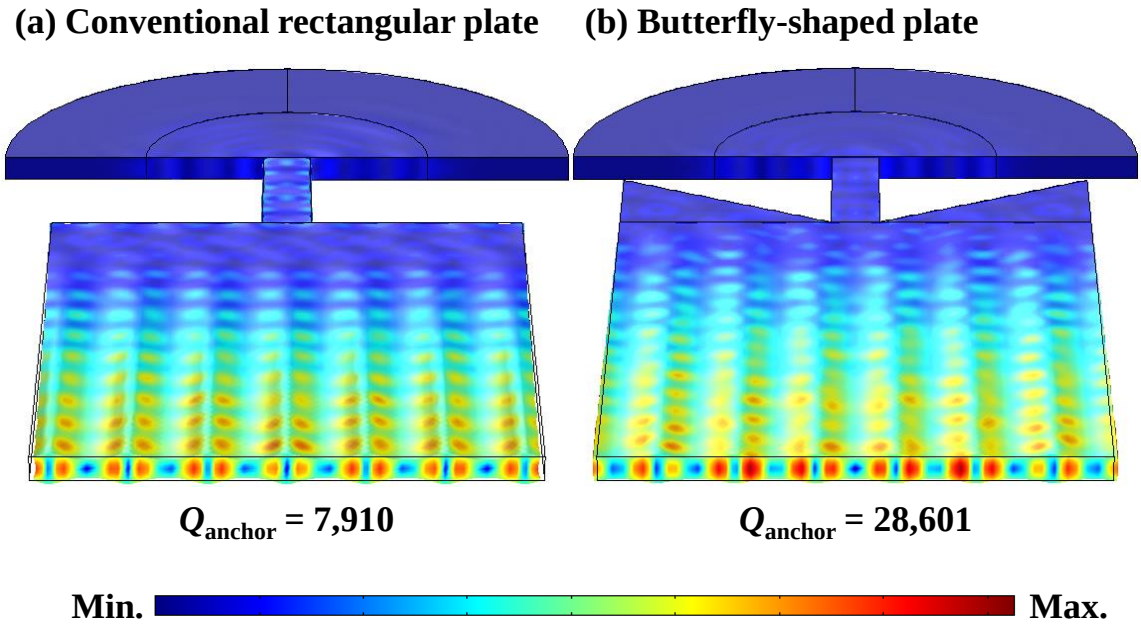

Figure.4-3. Resonance mode shapes (displacement profile) of (a) a conventional rectangular AlN plate with tether-to-plate angle α = 90º and (b) a butterfly-shaped AlN plate with α = 59º.

vibration. The predicated Q_{anchor} is equal to 7,910 based on the PML-based FEA model. In addition, Figure 4-3 (b) depicts the mode shape of the same S_0 mode at resonance in the butterfly-shaped AlN plate and the displacement in the tether is apparently less than that in the conventional rectangular plate. The simulated Q_{anchor} of the S_0 mode in the butterfly-shaped AlN plate is increased to 28,601. Interestingly, the butterfly-shape plate can effectively reduce the displacement occurring in the tethers and further offer a 3.62× improvement in the Q_{anchor}.

3.3 Experimental Results and Discussions

All the resonators reported in this work were fabricated on the same wafer and placed in the vicinity. The Lamb wave resonators were tested in air and S_{11} parameters were extracted using an Agilent E5071B network analyzer. The measured Q was extracted from the admittance plot by dividing the resonance frequency (f_s) by the 3 dB bandwidth.

The Q's measured from Lamb wave resonators using the butterfly-shaped plates are consistently higher than those using the rectangular plates. Fig. 5 compares one set of the measured frequency responses of the resonators with 13 finger electrodes on the 4-μm-thick rectangular and butterfly-shaped AlN plates. The 863.6 MHz resonator on the butterfly-shaped plate with α = 59º yields a Q of 2,433, representing a 1.27× enhancement over the 862.0 MHz resonator on the rectangular plate. An effective coupling (k_{eff}^2) of the butterfly-shaped resonator is 0.3%, slightly lower than 0.34%

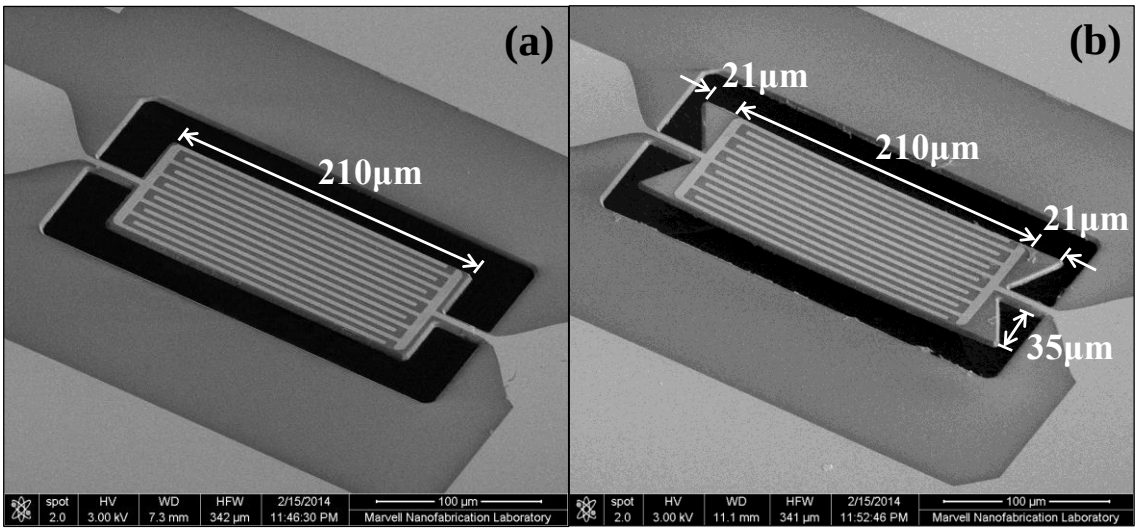

Figure 4-4. SEM images of the fabricated AlN Lamb wave resonators utilizing the (a) rectangular plate and (b) butterfly-shaped plate with $\alpha = 59^{\circ}$.

observed in the rectangular one, but the k_{eff}^2 is still sufficient for oscillators, sensors and narrowband filters. Moreover, the butterfly-shaped AlN plate neither introduces any other spurious mode nor shifts the resonance frequency significantly in comparison to the Lamb wave resonator with biconvex free edges 68.

Table 2 summarizes the performance of the AlN Lamb wave resonators on the rectangular and butterfly-shaped plates, including the six extracted modified Butterworth-Van Dyke (MBVD) 56 parameters as well as the loaded and unloaded Q. The extracted R_m of the conventional and butterfly-shaped AlN Lamb wave resonators are 256 Ω and 202 Ω, respectively. The resonator based on the butterfly-shaped plate exhibits a smaller R_m than the conventional resonator thanks to the higher Q. It should be noted that the series resistance (R_s) in the resonators is huge, implying imperfect metal contact

Table 4-2: Performance of the AlN Lamb wave resonators.

	Conventional	**Butterfly-shaped**
Motional resistance, R_m	256 Ω	202 Ω
Motional inductance, L_m	128.27 µH	168.06 µH
Motional capacitance, C_m	0.2658 fF	0.2021 fF
Static capacitance, C_0	96.39 fF	83.06 fF
Static resistance, R_0	268 Ω	321 Ω
Series resistance, R_s	193 Ω	193 Ω
Loaded Q	1,916	2,433
Unloaded Q	3,360	4,758
Simulated Q_{anchor}	7,910	28,601
Extracted Q_{other}	5,841	5,707

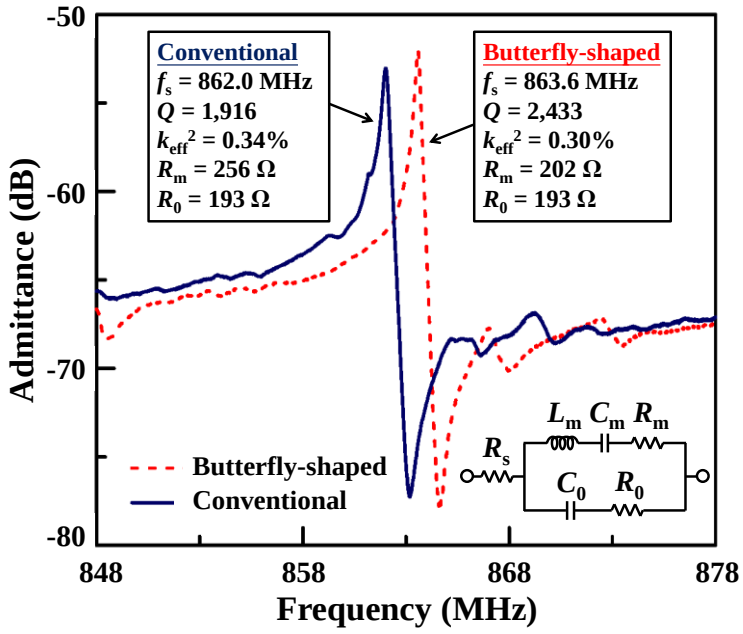

Figure 4-5. Measured admittance spectra of the conventional and butterfly-shaped AlN Lamb wave resonators. The inset depicts the MBVD model.

condition and poor metal deposition in the resonators, resulting in a considerable loading effect on *Q*'s. The unloaded *Q* of the butterfly-shaped resonator is 4,758, showing a 1.42× increase in the unloaded *Q* compared to the conventional Lamb wave resonator.

As listed in Table 4-2, based on the loaded *Q* and simulated Q_{anchor}, the extracted Q_{other} are around 5,800 for both resonators, implying that either the conventional resonator or the butterfly-shaped resonator are suffered from the same level of the other loss mechanisms. As a result, although the Q_{anchor} of the Lamb wave resonator has been boosted to 28,601 using the butterfly-shaped plate, the measured *Q* is still limited by the other loss mechanisms. Among all the loss mechanisms, the interfacial damping is suspected of another main loss mechanism in the AlN Lamb wave resonator since the Pt/Cr metal contact in the resonators is not perfect as discussed above 56, 62–64.

3.5 Conclusions

A new design approach for improving the anchor loss of the Lamb wave resonators is presented. By using the butterfly-shape AlN plate, the displacement in the tethers is efficiently suppressed and the energy loss via the tethers is then reduced. The butterfly-shaped resonator enables an unloaded *Q* up to 4,758, showing a 1.42× enhancement over the conventional resonator. In addition, the experimental results are in good agreement with the simulated predictions by the 3D PML-based FEA model, confirming that the butterfly-shaped AlN thin plate can efficiently eliminate the anchor dissipation. The *Q* of

the Lamb wave resonators is expected to be significantly increased using the butterfly-shaped plate if the interfacial loss can be minimized by well-controlled interface stresses under optimized metal deposition conditions.

Chapter 5

Conclusions

The piezoelectric AlN LWRs present a promising resonator technology which offers post-CMOS compatibility, multiple frequencies on a single chip, small size, low motional impedance, medium k_{eff}^2 and medium Q. The AlN LWRs show prospects to revolutionize the current wireless communication systems, such as the application in the frequency references or bandpass filters. Enjoying the merits of both SAW resonator and FBAR, the low deposition temperature of the AlN thin film and the Si-based fabrication processes of the LWRs show potential integration with the CMOS circuits, and the AlN LWRs can offer multiple frequencies on one die for future realization of a single chip RF front-end. Moreover, the LWRs present a superior in low motional resistances to the electrostatic resonators, allowing interfacing with the standard 50 Ω RF systems. In order to enhance the performance of the electronic system, the integration of micromechanical resonators directly onto the circuitry is an excellent approach to avoid unnecessary energy loss. However, the AlN Lamb wave resonator usually shows a Q below 2,000 due to complicated energy dissipation mechanisms, so an improvement in its Q is highly desirable to further enable low-loss filters, and low-phase-noise oscillators.

Different loss mechanisms in piezoelectric MEMS resonators have been investigated, and the anchor loss, representing the acoustic energy leakage via the support tethers into the substrates [14]–[21], are now suspected of the primary energy dissipation mechanisms. By suppressing the acoustic wave leakage through the tethers, the Q of the piezoelectric resonators can be improved. A new design approach for improving the anchor loss of the Lamb wave resonators has been presented in this report. By using the butterfly-shape AlN plate, the displacement in the tethers is efficiently suppressed and the energy loss via the tethers is then reduced. The butterfly-shaped resonator enables an unloaded Q up to 4,758, showing a 1.42× enhancement over the conventional resonator. In addition, the experimental results are in good agreement with the simulated predictions by the 3D PML-based FEA model.

Bibliography

1. C. T.-C. Nguyen, “MEMS technology for timing and frequency control,” *IEEE Trans. Ultrason. Ferroelectr. Freq. Control*, vol. 54, pp. 251–270, Feb. 2007.
2. J. Wang, Z. Ren, and C. T.-C. Nguyen, “1.156-GHz self-aligned vibrating micromechanical disk resonator,” *IEEE Trans. Ultrason. Ferroelectr. Freq. Control*, vol. 51, pp. 1607–1628, Dec. 2004.
3. V. Yantchev and I. Katardjiev, “Micromachined thin film plate acoustic resonators utilizing the lowest order symmetric Lamb wave mode,” *IEEE Trans. Ultrason. Ferroelectr. Freq. Control*, vol. 54, pp. 87–95, Jan. 2007.
4. S. Gong, N.-K. Kuo, and G. Piazza, “GHz high-*Q* lateral overmoded bulk acoustic-wave resonators using epitaxial SiC thin film,” *J. Microelectromech. Syst.*, vol. 21, pp. 253–255, Apr. 2012.
5. C.-M. Lin, Y.-Y. Chen, V. V. Felmetsger, D. G. Senesky, and A. P. Pisano, “AlN/3C–SiC composite plate enabling high-frequency and high-*Q* micro-mechanical resonators,” *Adv. Mater.*, vol. 24, pp.2722–2727, May 2012.
6. V. Kaajakari, T. Mattila, A. Oja, J. Kiihamäki, and H. Seppä, “Square-extensional mode single-crystal silicon micromechanical resonator for low-phase-noise oscillator applications,” *IEEE Electron Device Lett.*, vol. 25, pp.173–175, Apr. 2004.
7. Y.-W. Lin, S. Lee, S.-S. Li, Y. Xie, Z. Ren, and C. T.-C. Nguyen, “Series-resonant VHF micromechanical resonator reference oscillators,” *IEEE J. Solid-State Circuits*, vol. 39, pp.2477–2491, Dec. 2004.
8. C. Zuo, J. Van der Spiegel, and G. Piazza, “1.05-GHz CMOS oscillator based on lateral-field-excited piezoelectric AlN contour-mode MEMS resonators,” *IEEE Trans. Ultrason. Ferroelectr. Freq. Control*, vol. 57, pp. 82–87, Jan. 2010.
9. M. Rinaldi, C. Zuo, J. Van der Spiegel, and G. Piazza, “Reconfigurable CMOS oscillator based on multi-frequency AlN contour-mode resonators,” *IEEE Trans. Electron Devices*, vol. 58, pp. 1281–1286, May 2010.
10. W. Pang, R. C. Ruby, R. Parker, P. W. Fisher, M. A. Unkrich, and J. D. Larson, III, “A temperature-stable film bulk acoustic wave oscillator,” *IEEE Electron Device Lett.*, vol. 20, pp.315–318, Apr. 2008.
11. R. C. Ruby, M. Small, F. Bi, D. Lee, L. Callaghan, R. Parker, and S. Ortiz, “Positioning FBAR technology in the frequency and timing domain,” *IEEE Trans. Ultrason. Ferroelectr. Freq. Control*, vol. 59, pp. 334–345, Mar. 2012.
12. M. A. Schmidt and R. T. Howe, “Silicon resonant microsensors,” *Ceram. Eng. Sci. Proc.*, vol. 8, pp. 1019–1034, Oct. 1987.

13. W. C. Tang, T.-C. H. Nguyen, and R. T. Howe, "Laterally driven polysilicon resonant microstructures," *Sens. Actuators*, vol. 20, pp. 25–32, Nov. 1989.

14. C. T.-C. Nguyen and R. T. Howe, "An integrated CMOS micromechanical resonator high-*Q* oscillator," *IEEE J. Solid-State Circuits*, vol. 34, pp.440–455, Apr. 1999.

15. J. R. Clark, W.-T. Hsu, and C. T.-C. Nguyen, "High-*Q* VHF micromechanical contour-mode disk resonators," in *Tech. Dig. IEEE Intl. Electron Devices Mtg.*, 2000, pp. 493–496.

16. J. R. Clark, W.-T. Hsu, M. A. Abdelmoneum, and C. T.-C. Nguyen, "High-*Q* UHF micromechanical radial-contour mode disk resonators," *J. Microelectromech. Syst.*, vol. 14, pp. 1298–1310, Dec. 2005.

17. A. Ballato, "Piezoelectricity: history and new thrusts," in *Proc. IEEE Intl. Ultrason. Symp.*, 1996, pp. 575–583.

18. B. Drafts, "Acoustic wave technology sensors," *IEEE Trans. Microw. Theory Tech.*, vol. 49, pp. 795–802, Apr. 2001.

19. L. Rayleigh, "On waves propagated along the plane surface on an elastic solid," *Proc. London Math. Soc.*, vol. 17, pp. 4–11, Nov. 1885.

20. R. M. White and F. W. Voltmer, "Direct piezoelectric coupling to surface elastic waves," *Appl. Phys. Lett.*, vol. 7, pp. 314–316, Dec. 1965.

21. R. Weigel, D. P. Morgan, J. M. Owens, A. Ballato, K. M. Lakin, K. Hashimoto, and C. C. W. Ruppel, "Microwave acoustic materials, devices, and applications," *IEEE Trans. Microw. Theory Tech.*, vol. 50, pp. 738–749, Mar. 2002.

22. M. Werner, S. Klose, F. Szücs, Ch. Moelle, H. J. Fecht, C. Johnston, P. R. Chalker, and I. M. Buckley-Golder "High temperature Young's modulus of polycrystalline diamond," *Diam. Relat. Mater.*, vol. 6, pp. 344–347, Mar. 1997.

23. T.-T. Wu and Y.-Y. Chen, "Exact analysis of dispersive SAW devices on ZnO/diamond/Si layered structures," *IEEE Trans. Ultrason. Ferroelect. Freq. Control*, vol. 49, pp. 142–149, Jan. 2002.

24. M. El Hakiki, O. Elmazria, M. B. Assouar, V. Mortet, L. Le Brizoual, M. Vanecek, and P. Alnot "ZnO/AlN/diamond layered structure for SAW devices combining high velocity and high electromechanical coupling coefficient," *Diam. Relat. Mater.*, vol. 14, pp. 1175–1178, Mar.–Jul. 2005.

25. M. Benetti, D. Cannata, F. Di Pietrantonio, and E. Verona, "Growth of AlN piezoelectric film on diamond for high-frequency surface acoustic wave devices," *IEEE Trans. Ultrason. Ferroelectr. Freq. Control*, vol. 52, pp. 1806–1811, Oct. 2005.

26. C.-M. Lin, T.-T. Wu, Y.-Y. Chen, and T.-T. Chou, "Improved frequency responses of SAW filters with interdigitated interdigital transducers on ZnO/Diamond/Si layered structure," *J. Mech.* vol. 23, pp. 253–259, Sept. 2007.

27. K. Hashimoto, Ed., *RF Bulk Acoustic Wave Filters for Communications*, Norwood: Artech House, 2009.

28. W. H. Horton and R. C. Smythe, “On the trapped-wave criterion for AT-cut quartz resonators with coated electrodes,” *Proc. IEEE*, pp. 598–599, Apr. 1967.

29. K. M. Lakin, G. R. Kline and K. T. McCarron, “High-*Q* microwave acoustic resonators and filters,” *IEEE Trans. Microw. Theory Tech.*, vol. 41, pp. 2139–2146, Dec. 1993.

30. W. E. Newell, “Face-mounted piezoelectric resonators,” *Proc. IEEE*, pp. 575–581, Jun. 1965.

31. E. Klier, “Fundamental extensional mode of circular quartz plates,” *Czech. J. Phys.*, vol. 3, pp. 72–82, Mar. 1953.

32. J. Hermann and C. Bourgeois, “A new quartz crystal cut for contour mode resonators,” in *Proc. IEEE Intl. Freq. Control Symp.*, 1979, pp. 255–262.

33. S. C. Hight and G. W. Willard, “A simplified circuit for frequency substandards employing a new type of low-frequency zero-temperature-coefficient quartz crystal,” *Proc. Inst. Radio Eng.*, vol. 25, pp. 549–563, May 1937.

34. W. P. Mason, “A new quartz-crystal plate, designated the GT which produces a very constant frequency over a wide temperature range,” *Proc. Inst. Radio Eng.*, vol. 28, pp. 220–223, May 1940.

35. G. Piazza and A. P. Pisano, “Dry-released post-CMOS compatible contour-mode aluminum nitride micromechanical resonators for VHF applications,” in *Tech. Dig. Solid-State Sens. Actuators Microsyst. Workshop*, 2004, pp. 37–40.

36. G. Piazza, P. J. Stephanou, and A. P. Pisano, “Piezoelectric aluminum nitride vibrating contour-mode MEMS resonators,” *J. Microelectromech. Syst.*, vol. 15, pp. 1406–1418, Dec. 2006.

37. G. Piazza, P. J. Stephanou, and A. P. Pisano, “Single-chip multiple-frequency AlN MEMS filters based on contour-mode piezoelectric resonators,” *J. Microelectromech. Syst.*, vol. 16, pp. 319–328, Apr. 2007.

38. K. Toda, “Lamb-wave delay lines with interdigital electrodes,” *J. Appl. Phys.*, vol. 44, pp. 56–62, Jan. 1973.

39. A. J. Slobodnik Jr., E. D. Conway1 and R. T. Delmonico, “Microwave Acoustics Handbook,” *J. Acoust. Soc. Am.*, vol. 56, 1307, 1974.

40. R. M. White and S. W. Wenzel, “Fluid loading of a Lamb wave sensor,” *Appl. Phys. Lett.*, vol. 52, pp. 1653–1655, May 1988.

41. J. Bjurström, I. Katardjiev, and V. Yantchev, “Lateral-field-excited thin-film Lamb wave resonator,” *Appl. Phys. Lett.*, vol. 86, 154103, Apr. 2005.

42. J. Bjurström, I. Katardjiev, and V. Yantchev, “Thin film Lamb wave resonant structure – the first approach,” *Solid-State Electron.*, vol. 50, pp. 322–326, Mar. 2006.

43. V. Yantchev, and I. Katardjiev, “Micromachined thin film plate acoustic resonators utilizing the lowest order symmetric Lamb wave mode,” *IEEE Trans. Ultrason. Ferroelect. Freq. Control*, vol. 54, pp. 87–95, Jan. 2007.

44. V. Yantchev, L. Arapan, and I. Katardjiev, "Micromachined thin film plate acoustic resonators (FPAR): Part II," *IEEE Trans. Ultrason. Ferroelect. Freq. Control*, vol. 56, pp. 2701–2710, Dec. 2009.
45. P. J. Stephanou and A. P. Pisano, "800 MHz low motional resistance contour-extensional aluminum nitride micromechanical resonators," in *Tech. Dig. Solid-State Sens. Actuators Microsyst. Workshop*, 2006, pp. 60–61.
46. G. Piazza, P. J. Stephanou, and A. P. Pisano, "One and two port piezoelectric higher order contour-mode MEMS resonators for mechanical signal processing," *Solid-State Electron.*, vol. 51, pp. 1596–1608, 2007.
47. M. Rinaldi, C. Zuniga, C. Zuo, and G. Piazza, "Super-high-frequency two-port AlN contour-mode resonators for RF applications," *IEEE Trans. Ultrason. Ferroelect. Freq. Control*, vol. 57, pp. 38–45, Jan. 2010.
48. C. Zuo, N. Sinha, J. Van der Spiegel, and G. Piazza, "Multifrequency Pierce oscillator based on piezoelectric AlN contour-mode MEMS technology," *J. Microelectromech. Syst.*, vol. 19, pp. 570–580, Jun. 2010.
49. C.-M. Lin, Y.-J. Lai, T.-T. Yen, J.-C. Hsu, Y.-Y. Chen, D. G. Senesky, and A. P. Pisano, "Quality factor enhancement in Lamb wave resonators utilizing AlN plates with convex edges," in *Tech. Dig. Intl. Conf. Solid-State Sens. Actuators Microsyst.*, 2011, pp. 1512–1515.
50. J. Bjurström, G. Wingqvist, V. Yantchev and I. Katardjiev, J. Micromech. Microeng, **17**, 651 (2007).
51. C. T.-C. Nguyen, "MEMS technology for timing and frequency con- trol," *IEEE Trans. Ultrason. Ferroelect. Freq. Control*, vol. 54, pp. 251–270, Feb. 2007.
52. V. Yantchev and I. Katardjiev, "Thin film Lamb wave resonators in frequency control and sensing applications: a review," *J. Micromech. Microeng.*, vol. 23, 043001, Apr. 2013.
53. G. Piazza, P.J. Stephanou, A.P. Pisano, "Piezoelectric Aluminum nitride vibrating contour-mode MEMS resonators," *J. Microelectromech. Syst.*, vol. 15, pp. 1406–1418, Dec. 2006.
54. C.-M. Lin, T.-T. Yen, Y.-J. Lai, V. V. Felmetsger, M. A. Hopcroft, J. H. Kuypers, and A. P. Pisano, "Temperature-compensated aluminum nitride Lamb wave resonators," *IEEE Trans. Ultrason. Ferroelectr. Freq. Control*, vol. 57, pp. 524–532, Mar. 2010
55. C.-M. Lin, T.-T. Yen, V. V. Felmetsger, M. A. Hopcroft, J. H. Kuypers, and A. P. Pisano, "Thermally compensated aluminum nitride Lamb wave resonators for high temperature applications," *Appl. Phys. Lett.*, vol. 97, 083501, Aug. 2010.
56. C.-M. Lin, V. Yantchev, J. Zou, Y.-Y. Chen, and A. P. Pisano, "Micromachined one-port aluminum nitride Lamb wave resonators utilizing the lowest-order symmetric mode," *J. Microelectromech. Syst.*, vol. 23, pp. 78–91, Feb. 2014.
57. J. Zou, C.-M. Lin, Y.-Y. Chen, and A. P. Pisano, "Theoretical study of thermally stable SiO_2/AlN/SiO_2 Lamb wave resonators at high temperatures," *J. Appl. Phys.*, vol. 115, 094510, Mar. 2014.

58. C.-M. Lin , Y.-Y. Chen , V. V. Felmetsger, D. G. Senesky, and A. P. Pisano, "AlN/3C–SiC composite plate enabling high-frequency and high-*Q* micromechanical esonators," *Adv. Mater.*, vol. 24, pp. 2722–2727, May 2012.
59. C.-M. Lin, Y.-Y. Chen, and A. P. Pisano, "Theoretical investigation of Lamb wave characteristics in AlN/3C–SiC composite membranes," *Appl. Phys. Lett.*, vol. 97, 193506, Nov. 2010.
60. W.-C. Li, Y. Lin, B. Kim, Z. Ren, and C. T.-C. Nguyen, "Quality factor enhancement in micromechanical resonators at cryogenic temperatures," in *Proc. Int. Conf. Solid-State Sens. Actuators Microsyst.*, Denvor, CO, Jun. 2009, pp. 1445–1448.
61. S. Ghaffari, S. A. Chandorkar, S. Wang, E. J. Ng, C. H. Ahn, V. Hong, Y. Yang, and T. W. Kenny, "Quantum limit of quality factor in silicon micro and nano mechanical resonators," *Sci. Rep.*, vol. 3, 3244, Nov. 2013.
62. Z. Hao and B. Liao, "An analytical study on interfacial dissipation in piezoelectric rectangular block resonators with in-plane longitudinal-mode vibrations," *Sens. Actuators A: Phys.*, vol. 163, pp.401–409, Sept. 2010.
63. T.-T. Yen, A. P. Pisano, and C. T.-C. Nguyen, "High-*Q* capacitive-piezoelectric AlN Lamb wave resonators," in *Proc. IEEE Int. Conf. Micro Electro Mech. Syst.*, Taipei, Taiwan, Jan. 2013, pp. 114–117.
64. A. Frangia, M. Cremonesia, A. Jaakkolab, and T. Pensala, "Analysis of anchor and interface losses in piezoelectric MEMS resonators," *Sens. Actuators A: Phys.*, vol. 190, pp.127–135, Feb. 2013.
65. L. Wu, M. Akgul, Z. Ren, Y. Lin, W.-C. Li, and C. T.-C. Nguyen, "Hollow stems for higher micromechanical disk resonator quality factor", in *Proc. IEEE Intl. Ultrason. Symp.*, Orlando, FL, Oct. 2011, pp. 1964–1967.
66. W. Pang, H. Zhang, S. Whangbo, and E.S. Kim, "High Q film bulk acoustic resonator from 2.4 to 5.1 GHz," in *Proc. IEEE Int. Conf. Micro Electro Mech. Syst.*, Maastricht, Netherlands, Jan. 2004, pp. 805–808.
67. B. P. Harrington and R. Abdolvand, "In-plane acoustic reflectors for reducing effective anchor loss in lateral-extensional MEMS resonators," *J. Micromech. Microeng*., vol. 21, 085021, Aug. 2011.
68. C.-M. Lin, Y.-J. Lai, J.-C. Hsu, Y.-Y. Chen, D. G. Senesky, and A. P. Pisano, "High-*Q* aluminum nitride Lamb wave resonators with biconvex edges," *Appl. Phys. Lett.*, vol. 99, 143501, Oct. 2011.
69. Y.-Y. Chen, Y.-T. Lai, and C.-M. Lin, "Finite element analysis of anchor loss in AlN Lamb wave resonators," in *Proc. IEEE Int. Freq. Contr. Symp.*, Taipei, Taiwan, 2014, pp. 132–136.
70. C. Cassella, J. S. Fernandez, M. Cremonesi, A. Frangi, and G. Piazza, "Reduction of anchor losses by etched slots in aluminum nitride contour mode resonators," in *Proc. Eur. Freq. Time Forum & IEEE Int. Freq. Contr. Symp.*, Prague, Czech, 2013, pp. 926–929.
71. C.-M. Lin, J.-C. Hsu, D. G. Senesky, and A. P. Pisano, "Anchor loss reduction in AlN Lamb wave resonators using phononic crystal strip tethers", in *Proc. IEEE Int. Freq. Contr. Symp.*, Taipei, Taiwan, 2014, pp. 371–375.

72. D. S. Bindel and S. Govindjee, “Elastic PMLs for resonator anchor loss simulation,” *Int. J. Numer. Meth. Engng.*, vol. 64, pp. 798–818, Oct. 2005.